Aerospace Science and Technology 41 (2015) 274–288

Contents lists available at ScienceDirect

Aerospace Science and Technology

www.elsevier.com/locate/aescte

Rarefied gas flow simulations of NACA 0012 airfoil and sharp 25–55-deg biconic subject to high order nonequilibrium boundary conditions in CFD

Nam T.P. Le [a,b], Ahmad Shoja-Sani [c], Ehsan Roohi [c,*,1]

[a] Division of Computational Mathematics and Engineering, Institute for Computational Science, Ton Duc Thang University, Ho Chi Minh City, Viet Nam
[b] Faculty of Civil Engineering, Ton Duc Thang University, Ho Chi Minh City, Viet Nam
[c] High Performance Computing (HPC) Laboratory, Department of Mechanical Engineering, Faculty of Engineering, Ferdowsi University of Mashhad, P.O. Box 91775-1111, Mashhad, Iran

ARTICLE INFO

Article history:
Received 28 August 2014
Received in revised form 3 December 2014
Accepted 21 December 2014
Available online 6 January 2015

Keywords:
Second order slip/jump boundary conditions
DSMC
NACA 0012 airfoil
Biconic geometry
OpenFOAM

ABSTRACT

The NACA 0012 airfoil and the sharp 25–55-deg biconic cases are usually considered in evaluating the accuracy of new forms of velocity slip and temperature jump wall boundary conditions in the Navier–Stokes–Fourier equations. These cases have been investigated by many researchers in previous works with the first order Maxwell slip and Smoluchowski jump boundary conditions. Recently, we proposed a new form of the second order temperature jump for simulating rarefied gas flows and obtained accurate results for low-speed microflows. The current work is an extension of our previous CFD work where we applied both the second order velocity slip condition and the second order temperature jump boundary condition in new forms to simulate rarefied external gas flows for these cases. The second order boundary conditions are implemented into the *rhoCentralFoam* solver in the OpenFOAM software. The NACA 0012 airfoil case is investigated with angles-of-attack of 0 and 10 degrees and Mach numbers of 0.8 and 2. The sharp 25–55-deg biconic case is simulated at Mach of 15.6. The simulation results obtained for the NACA 0012 airfoil show that the combination of the second order slip/jump boundary conditions gives suitable agreements with DSMC for surface gas temperature and drag coefficients in comparison with those of the first order conditions. However, the results of the biconic case figure out that the second order conditions are not superior to the first order conditions.

© 2014 Elsevier Masson SAS. All rights reserved.

1. Introduction

The accurate simulation of nonequilibrium rarefied gas flows remains very challenging in the field of computational fluid dynamics (CFD) in the design, analysis, and optimization of flight systems [1,2]. Nonequilibrium of a rarefied gas flow in micro/nano-devices or hypersonic vehicles can be characterized by the Knudsen number, Kn, that is the ratio of the molecular mean free path, λ, to the characteristic length of their geometry, l. If the gas density is relatively high and Kn is very small, i.e., continuum regime, gas flows may be simulated by solving the Navier–Stokes–Fourier (N-S-F) equations with no-slip boundary conditions ($\mathrm{Kn} < 0.001$). The lack of collisions means the N-S-F equations become inappropriate in rarefied regimes indicated by a large Knudsen number. An approach to improving the N-S-F equations in the range of $0.001 < \mathrm{Kn} < 0.1$, i.e. slip regime, is to use velocity slip and temperature jump boundary conditions. However, as Kn rises into the range $0.1 < \mathrm{Kn} < 10$, that is called the transition regime, the N-S-F equations become inappropriate because the near-equilibrium fluid assumption for flows has broken down. For $\mathrm{Kn} > 10$, the flow is called to be in the free molecular regime. Computational simulations of nonequilibrium rarefied gas flows require knowledge of the kinetic theory of gases and an understanding of different numerical simulation methods such as CFD, Direct Simulation Monte-Carlo (DSMC), and hybrid CFD–DSMC. Typical methods used to simulate hypersonic gas flows are DSMC and CFD. The DSMC method has successfully simulated hypersonic gas flows in all the different regimes presented by Kn, but the computational effort is quite expensive; especially for three-dimensional flows. The computational effort of CFD is much less than the DSMC method.

The design of re-entry or air vehicles requires accurate prediction of the surface properties in flight such as surface temperature, pressure, heat transfer and shear stress. In this paper, two typical configurations are numerically examined: NACA 0012 micro-airfoil

* Corresponding author. Tel.: +98 (51) 38805136; fax: +98 (51) 38763304.
E-mail addresses: letuanphuongnam@tdt.edu.vn (N.T.P. Le), e.roohi@ferdowsi.um.ac.ir (E. Roohi).
[1] Assistant Professor.

http://dx.doi.org/10.1016/j.ast.2014.12.019
1270-9638/© 2014 Elsevier Masson SAS. All rights reserved.

[3,4] and a sharp 25–55-deg biconic using the CFD method within the OpenFOAM framework [5]. The CFD solver "rhoCentralFoam" in the OpenFOAM [5] which solves the N-S-F equations with the slip and jump boundary conditions is selected for performing all our CFD simulations. In this solver, the N-S-F equations are numerically solved with the high-resolution central scheme described in [6]. The open source CFD software, OpenFOAM, uses the finite volume numeric to solve systems of partial differential equations ascribed on any three-dimensional unstructured mesh of polygonal cells. The first configuration, the NACA 0012 airfoil with the chord length of 4 cm is chosen to investigate numerically rarefied gas flows around an airfoil. This airfoil holds a basic shape and is appropriate as a starting point to study the aerodynamic features of micro vehicles [4]. Two Mach numbers, $M = 0.8$ and 2, and angles-of-attack (AOA), AOA = 0-deg and 10-deg, are considered. There are experimental data of the density field [7] and DSMC data [4,8] available to evaluate the present CFD results. Previous work found that there was a significant difference between the N-S-F and experimental density fields [7,9]. It was explained by omitting of a slip velocity along the airfoil surface in the N-S-F calculations. A further investigation at $M = 2.0$ and AOA = 0-deg showed that this difference may be considerably reduced if the slip velocity and temperature jump boundary conditions were included in the calculations [8,10,11]. The Sutherland and the constant viscosity models were adopted for CFD simulations in [8,10,11]. Moreover, this airfoil was also simulated by the Bhatnagar–Gross–Krook (BGK) model [12] and the Morse–Holway [13,14] model at $M = 2.0$. The density field given by the Morse–Holway model compared better with the experiment than that given by the BGK model [4].

The second configuration is the case of shock/shock interactions in the hypersonic gas flow over a sharp 25–55-deg biconic. Shock interactions are very commonly encountered in the hypersonic vehicle design because they can produce very high localized heating loads on the surface and potential damage the thermal protection system. Moreover, they have caused the flow to separate and alter the vehicle aerodynamic performance characteristics. Therefore, this case is a challenging test for evaluating the accuracy of numerical simulations, moreover, experimental data are available for validating the correctness of the numerical [15–17]. The biconic case has been carefully simulated by many researchers [5, 15,18–22] with DSMC and CFD. In the literature, the CFD simulations of the NACA 0012 airfoil and biconic cases were solved by the N-S-F equations accompanied with the first order Maxwell slip condition [23] and Smoluchowski jump condition [24]. In the present work, we investigate the Run 7 of the experiment of the biconic case at $M = 15.6$ reported in [16,17] as there are full set of experimental [16,17] and DSMC data [19] of the surface properties for comparison.

In summary, the focus of the present work is an assessment of CFD for the particular issue of shock interactions and surface properties of nonequilibrium gas flows. Consideration of surface slip/jump boundary conditions is essential for accurate calculation of the surface properties such as the surface velocity, surface temperature heat flux, and surface pressure for re-entry or micro air vehicle designs. Moreover, the accuracy of the full-field computational results depends on the surface boundary conditions applied. The appropriate treatment of the boundary conditions is critical when comparing DSMC or experimental data to the CFD results. In the present work, the rarefied gas flow in the slip regime ($0.01 < \mathrm{Kn} < 0.1$) is investigated, and we will revisit the first order Maxwell slip and Smoluchowski jump conditions in the CFD simulations. The Maxwell viscosity model [25] is adopted for all CFD simulations as this viscosity model gave good results for simulating one-dimensional shock wave structures compared with experimental data in [26]. *There is an extension of previous CFD work* in the present work that is we apply both the second order slip and second order jump conditions for two configurations mentioned above. In the literature, the combination of both the second order slip and second order jump conditions was only used for the BGK and Burnett equations in [27] for simulating the hypersonic gas flows. The second order slip condition [28,29] was developed following kinetic theory applied to rarefied gas microflows in *planar* surface geometries. Recently, a new form of the second order jump condition for simulating rarefied gas flows has been proposed in [30] and accurate results for microflows were obtained. *Here, for the first time the combination of both the second order slip and the second order jump conditions in a new form* is employed with the N-S-F equations for simulating rarefied gas flows around the NACA 0012 airfoil and sharp 25–55-deg biconic cases. The effect of the second order conditions on the behavior of rarefied gas flows for the both cases is numerically investigated in this work. The coefficients of the second order conditions are numerically adjusted to match DSMC or experimental data.

2. Governing Navier–Stokes–Fourier equations

In this section we present the governing equation and the nonequilibrium slip and jump boundary conditions, and transport models. The N-S-F equations are typically used to describe gas flows in the continuum fluid regime. Governing N-S-F equations neglecting body forces are expressed in the vector form as follows:

Conservation of mass

$$\frac{\partial \rho}{\partial t} + \nabla \cdot [\rho \mathbf{u}] = 0, \tag{1}$$

Conservation of momentum

$$\frac{\partial (\rho \mathbf{u})}{\partial t} + \nabla \cdot \big[\mathbf{u}(\rho \mathbf{u})\big] + \nabla p + \nabla \mathbf{\Pi} = 0, \tag{2}$$

Conservation of total energy

$$\frac{\partial (\rho E)}{\partial t} + \nabla \cdot \big[\mathbf{u}(\rho E)\big] + \nabla \cdot (\mathbf{u} p) + \nabla \cdot (\mathbf{\Pi} \cdot \mathbf{u}) + \nabla \cdot \mathbf{Q} = 0, \tag{3}$$

where ρ is gas density; p is the gas pressure; $\mathbf{u}$ is the velocity; E is total energy, $E = e + 0.5|\mathbf{u}^2|$; e is the internal energy per unit mass, $e = c_v T$; c_v is constant volume specific heat specific heat; T is temperature; $\mathbf{\Pi}$ is stress tensor and is computed as $\mathbf{\Pi} = -2\mu dev(\mathbf{D})$, where $(\mathbf{D}) = 0.5[\nabla \mathbf{u} + (\nabla \mathbf{u})^{\mathrm{T}}]$ and μ is the viscosity; *dev* denotes deviatoric of tensor $(\mathbf{D}) - (1/3)(\mathrm{tr})(\mathbf{D})\mathbf{I}$, where $\mathbf{I}$ is the identity tensor; tr is the trace of tensor; $\mathbf{Q}$ is the heat flux and is computed by the Fourier law, $\mathbf{Q} = -k\nabla T$; k is thermal conductivity. A calorically perfect gas is used for all CFD simulations, so $p = \rho R T$ where R is the specific gas constant. The N-S-F equations are implemented and solved numerically with the high-resolution central scheme described in [6] in OpenFOAM as the solver *rhoCentralFoam*.

3. Nonequilibrium slip and jump boundary conditions

The first order Maxwell slip boundary condition, including the effect of thermal creep, can be expressed in the vector form as [23]:

$$\mathbf{u} = -\left(\frac{2-\sigma_{\mathrm{u}}}{\sigma_{\mathrm{u}}}\right)\frac{\lambda}{\mu}\boldsymbol{\tau} - \frac{3}{4}\frac{\mathrm{Pr}(\gamma - 1)}{\gamma p}\mathbf{q} + \mathbf{u}_{\mathrm{w}}, \tag{4}$$

where the tangential shear stress is $\boldsymbol{\tau} = \mathbf{S} \cdot (\mathbf{n} \cdot \mathbf{\Pi})$ and the heat flux is $\mathbf{q} = \mathbf{Q} \cdot \mathbf{S}$ at the surface. Tensor $\mathbf{S} = \mathbf{I} - \mathbf{nn}$, where $\mathbf{n}$ is the unit normal vector defined as positive in the direction pointing out of the flow domain, removes normal components of any non-scalar field, e.g., velocity, so that slip only occurs in the direction tangential to the surface; λ is the mean free path; γ is the specific heat ratio; Pr is the Prandtl number; and $\mathbf{u}_{\mathrm{w}}$ is the

wall velocity. The tangential momentum accommodation coefficient determines the proportion of molecules reflected from the surface specularly (equal to $1-\sigma_u$) or diffusely (equal to σ_u), and $0 \le \sigma_u \le 1$. Substituting $\boldsymbol{\tau} = -\mathbf{S}\cdot(\mathbf{n}\cdot\boldsymbol{\Pi})$ and $\boldsymbol{\Pi} = \mu\nabla\mathbf{u} + \boldsymbol{\Pi}_{mc}$ with $\boldsymbol{\Pi}_{mc} = \mu((\nabla\mathbf{u})^T - (\frac{2}{3})\mathbf{I}\,\mathrm{tr}(\nabla\mathbf{u}))$ into Eq. (4), and noting that $\mathbf{S}\cdot\nabla_{\mathbf{n}}\phi \equiv \nabla_{\mathbf{n}}(\mathbf{S}\cdot\phi)$, Eq. (1) becomes:

$$\mathbf{u} + \left(\frac{2-\sigma_u}{\sigma_u}\right)\lambda\nabla_{\mathbf{n}}(\mathbf{S}\cdot\mathbf{u}) = \mathbf{u}_w - \left(\frac{2-\sigma_u}{\sigma_u}\right)\frac{\lambda}{\mu}\mathbf{S}\cdot(\mathbf{n}\cdot\boldsymbol{\Pi}_{mc}) - \frac{3}{4}\frac{\mu}{\rho}\frac{\mathbf{S}\cdot\nabla T}{T}. \tag{5}$$

The right-hand side of Eq. (5) contains three terms that are associated with (in order): the surface velocity, the so-called curvature effect [28,31], and thermal creep. For the first-order Maxwell slip condition, the accuracy of simulation results could be controlled by the tangential momentum accommodation coefficient, which varies from 0 to 1.0. The Maxwellian mean free path is defined as follows [25]:

$$\lambda = \frac{\mu}{\rho}\sqrt{\frac{\pi}{2RT}}, \tag{6}$$

where the viscosity μ is computed by the Maxwell model for two-dimensional gas [25]:

$$\mu = \sqrt{\frac{mk_B}{\pi}}\frac{1}{\pi d^2}T^{0.5}, \tag{7}$$

where m is mass of a gas molecule, $m = 46.5\times10^{-27}$ kg for nitrogen, and 48.1×10^{-27} kg for air [32]; d is diameter of gas molecules, $d = 4.17\times10^{-10}$ m for nitrogen, and 4.19×10^{-10} m for air [32]; and k_B is the Boltzmann constant. It is observed that the viscosity only depends on the temperature in the Maxwell viscosity model.

Experimental observations show that the temperature of a rarefied gas at the surface is not equal to the wall temperature, T_w. This difference is called the "temperature jump" and is driven by the heat flux normal to the surface. The Smoluchowski boundary condition can be written [24]:

$$T + \frac{2-\sigma_T}{\sigma_T}\frac{2\gamma}{(\gamma+1)\,\mathrm{Pr}}\lambda\nabla_{\mathbf{n}}T = T_w \tag{8}$$

The Smoluchowski condition also depends on the thermal accommodation coefficient, σ_T, which varies from 0 to 1.0, and decides the accuracy of the simulation results. The σ_T is used to describe the temperatures of the receding molecules. Specularly reflected molecules recede from the surface with their original incident energy, and diffusely reflected molecules have their energies adjusted to those would arise in a mass of gas in equilibrium at the temperature of the surface. Perfect heat exchange between gas molecules and a solid surface corresponds to $\sigma_T = 1$, and no heat exchange to $\sigma_T = 0$.

The second order velocity slip boundary condition for a *planar* surface can be expressed as follows [28,29]:

$$\mathbf{u} = -A_1\lambda\nabla_n(\mathbf{S}\cdot\mathbf{u}) - A_2\lambda^2\nabla_n^2(\mathbf{S}\cdot\mathbf{u}) + \mathbf{u}_w, \tag{9}$$

where A_1 and A_2 are the first and second order coefficients. It is assumed there is no more heat flux along the surface and the so-called curvature effect as in Eq. (5). The values A_1 and A_2 are proposed either from theory or experiment, and are still the subject of much discussion. If $A_2 = 0$, then the second order slip condition becomes the first order Maxwell slip condition with $\sigma_u = 1$.

Recently, we proposed a new form of the second order jump condition in [30] that is simpler than those in literature:

$$T = -\frac{2\gamma}{\gamma+1}\frac{1}{\mathrm{Pr}}\left(C_1\lambda\nabla_n T + C_2\lambda^2\nabla_n^2 T\right) + T_w \tag{10}$$

where C_1 and C_2 are the first and second order coefficients. It is seen that if $C_2 = 0$, then Eq. (10) becomes the first order Smoluchowski jump condition with $\sigma_T = 1$.

All boundary conditions expressed by Eqs. (5), (8), (9) and (10) are implemented into the solver *rhoCentralFoam* in OpenFOAM that the implementation of these boundary conditions was presented in detail in [31]. These conditions are used for simulating the airfoil and biconic cases in this work.

4. Slip and jump boundary conditions in DSMC

The surface boundary conditions in the DSMC method simulate gas–surface interactions: DSMC particles are adsorbed on the surface and then re-emitted. In fact, DSMC particles collide with the surface and experience both specular and diffuse interactions. The accommodation coefficients represent the fraction of incoming DSMC particles that are reflected diffusely, and the remainder are reflected specularly. Velocity slip and translational temperature jump are calculated with the accommodation coefficients of unity as presented in [32,33],

$$\mathbf{u}_s = \frac{\sum((m/u_n)u_p)}{\sum(m/u_n)} - \mathbf{u}_w, \tag{11}$$

$$T = \frac{\sum((m/u_n)\|\mathbf{u}\|) - \sum(m/u_n)\mathbf{u}_s^2}{3k\sum(1/u_n)} - T_w, \tag{12}$$

where u_n is the velocity normal to the surface; u_p is the velocity parallel to the surface; $\|\mathbf{u}\|$ is the velocity magnitude respectively. The u_n and u_p in the equations are taken prior to and after the collision with the surface, and the summations include pre- and post-collision molecules.

The heat flux is computed in DSMC as follows: [32]

$$\mathbf{Q} = \frac{1}{2}n\overline{mu'^2\mathbf{u}} + n\overline{e}\overline{\mathbf{u}}, \tag{13}$$

where n is the number density; m is molecular mass; u' is thermal velocity of a molecule; e is internal energy, and the symbol "overbar" denotes the mean value.

5. Numerical setups

The profile of the NACA 0012 airfoil is computed by the expression below [34]:

$$y = 0.6\left(0.2969\left(\frac{x}{c}\right)^{0.5} - 0.126\left(\frac{x}{c}\right) - 0.3537\left(\frac{x}{c}\right)^2 + 0.2843\left(\frac{x}{c}\right)^3 - 0.1015\left(\frac{x}{c}\right)^4\right), \tag{14}$$

where c is the chord length, $c = 4$ cm; x is the running distance along the chord ($0 \le x \le c$); y is the half thickness of the airfoil. The dimensions of geometries of the airfoil and biconic cases are presented in Figs. 1a and 2a, respectively. Numerical setups of computational domains for these two cases are presented in Figs. 1a and 2b. The computational domain of the biconic case is similar to that given in [20]. The structured C-type mesh is used for the airfoil case, as seen in Fig. 1b, and the final mesh is adapted from our previous work in [8] with 600 cells on the airfoil surface. For the supersonic airfoil case, $M = 2$, the values $L = 6c$ and $H = 3c$. For the subsonic airfoil case, $M = 0.8$, it is a transonic flow involves a flowfield of an elliptic character, presenting difficulties at the outer boundaries of the computational domain [4]. Therefore, a large computational domain is constructed by $L = H = 50c$

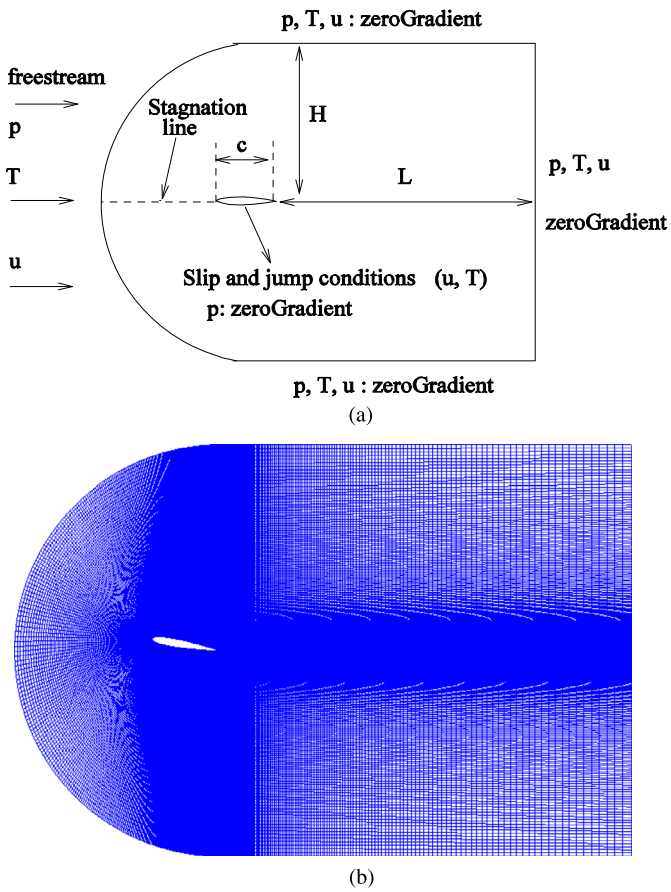

Fig. 1. (a) Geometry, dimensions and numerical setups of the NACA 0012 airfoil case. (b) Structured C-type mesh of the NACA 0012 airfoil case.

to remove the effect of the airfoil disturbances in the imposed boundary conditions [8]. In both cases, the nonequilibrium slip and jump boundary conditions are applied to the airfoil and biconic surfaces for the flow variables $(T, \mathbf{u})$. The boundary condition for the pressure, p, at the airfoil and biconic surfaces, is zero normal gradient. At the inflow boundary, the free stream conditions are maintained throughout the computational process. For the airfoil case, at the top, bottom and outflow boundaries, the gas flow is allowed to leave the computational domain. This condition specifies that normal gradients of flow variables $(p, T, \mathbf{u})$ vanish at these boundaries. For the biconic case, the zero normal gradients of the flow variables $(p, T, \mathbf{u})$ are set at the outflow boundary so that they vanish at this boundary. For the two-dimensional axisymmetric biconic case, the geometry is specified as a wedge of one cell thickness running along the plane of geometry. The axisymmetric wedge planes must be specified as separate patches of type "wedge", as seen in Fig. 2b. Structured mesh of the biconic case is presented in Fig. 2c. Free stream conditions and working gases of all cases are shown in Table 1.

6. Simulation results and discussions

In this section, the CFD simulation results with the first order and the second order slip and jump boundary conditions are presented and compared with DSMC and experimental data. The values $\sigma_u = \sigma_T = 1.0$ are used for all CFD simulations with the first order conditions and DSMC data. The combination of the second order slip and second order jump conditions is applied with various coefficients, A_1, A_2, C_1 and C_2. The purpose of the comparison between DSMC and CFD with the second order slip and jump conditions that is we assume that DSMC data is correct and do

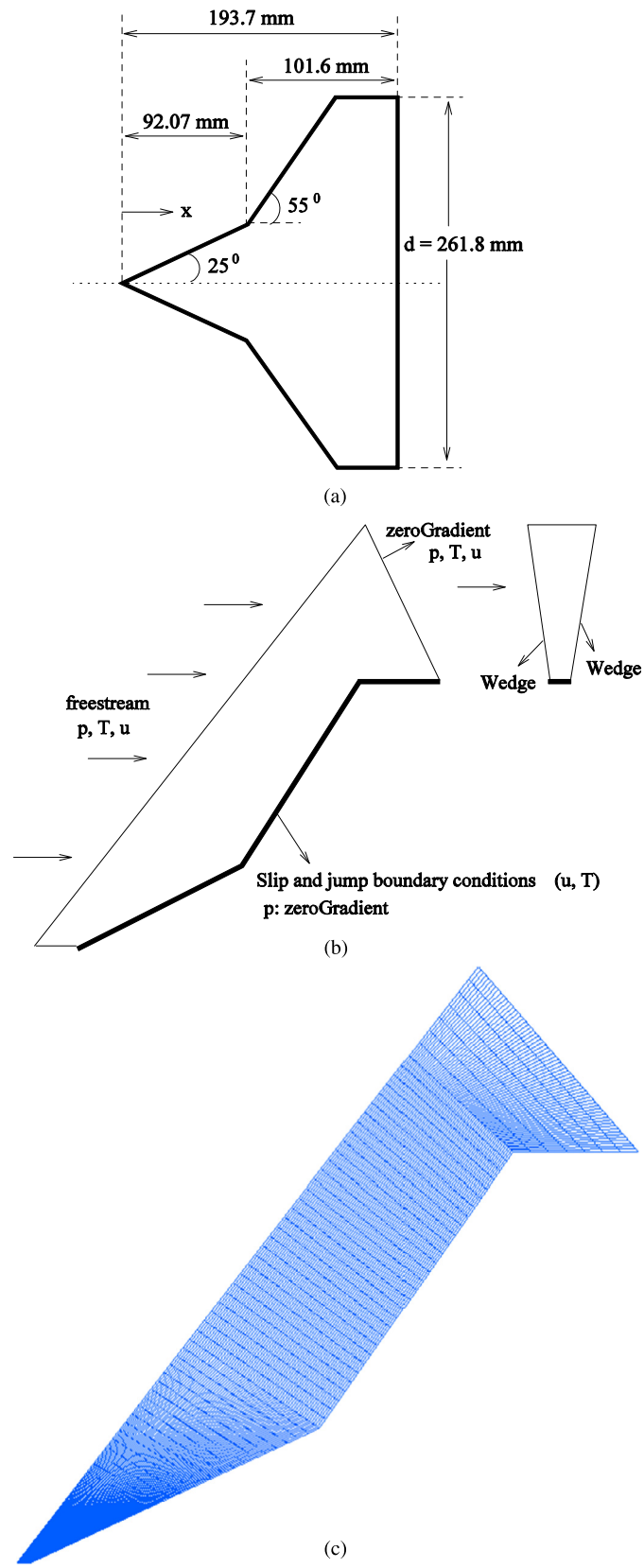

Fig. 2. (a) Geometry and dimensions of the sharp 25–55-deg biconic case. (b) Numerical setups of the sharp 25–55-deg biconic case. (c) Structured mesh of the sharp 25–55-deg biconic case, 256×256 (every fourth line presented).

Table 1
Free stream conditions and working gases of the NACA 0012 airfoil and sharp 25–55-deg biconic cases [4,8,17,19].

Case	p_∞ (Pa)	ρ_∞ (kg/m^3)	M_∞	$\mathbf{u}_\infty$ (m/s)	T_∞ (K)	T_w (K)	Gas	AOA (deg)	Kn
Airfoil	2.78443	6.026×10^{-5}	2	509	161	290	Air	0 and 10	0.026
Airfoil	8.23150	1.116×10^{-4}	0.8	257	257	290	Air	0	0.014
Biconic	2.23	1.757×10^{-4}	15.6	2073	42.6	297.2	N_2		

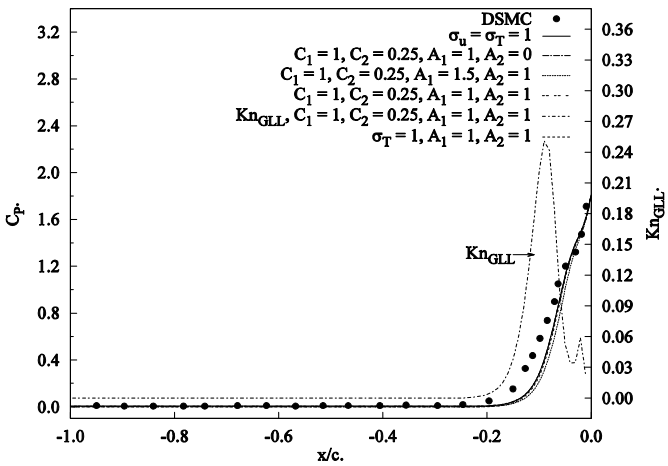

Fig. 3. Surface pressure coefficient, C_P, and Kn_{GLL} distributions along the stagnation line, $M = 2$, AOA = 0-deg, Kn = 0.026.

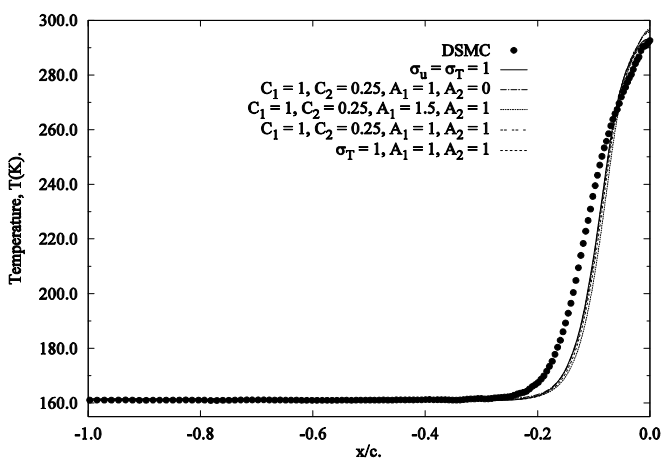

Fig. 4. Gas temperature distribution along the stagnation line, $M = 2$, AOA = 0-deg, Kn = 0.026.

numerical experiments for coefficients (A_1, A_2, C_1, C_2) to match DSMC data. For the NACA 0012 airfoil, the pressure coefficient, C_P, is presented in figures below and is computed from the free stream density, pressure and velocity (ρ_∞, p_∞, $\mathbf{u}_\infty$) and the surface pressure, p as follows:

$$C_p = \frac{p_w - p_\infty}{0.5\rho_\infty \mathbf{u}_\infty^2}. \tag{15}$$

The CFD results, DSMC and experimental data are plotted against the normalized distance, x/c, for the NACA 0012 airfoil case.

6.1. NACA 0012 airfoil case $M = 2$, Kn = 0.026, AOA = 0-deg

The simulations with the second order slip and jump conditions are run with various cases 1) $A_1 = 1$, $A_2 = 0$, $C_1 = 1$, $C_2 = 0.25$, 2) $A_1 = 1$, $A_2 = 1$, $C_1 = 1$, $C_2 = 0.25$, $A_1 = 1.5$, 3) $A_2 = 1$, $C_1 = 1$, $C_2 = 0.25$, and 4) $\sigma_T = 1$, $A_1 = 1$, $A_2 = 1$. Firstly, the simulation results along the stagnation line are presented. The supersonic air flow around the airfoil creates a bow shock. Along the stagnation

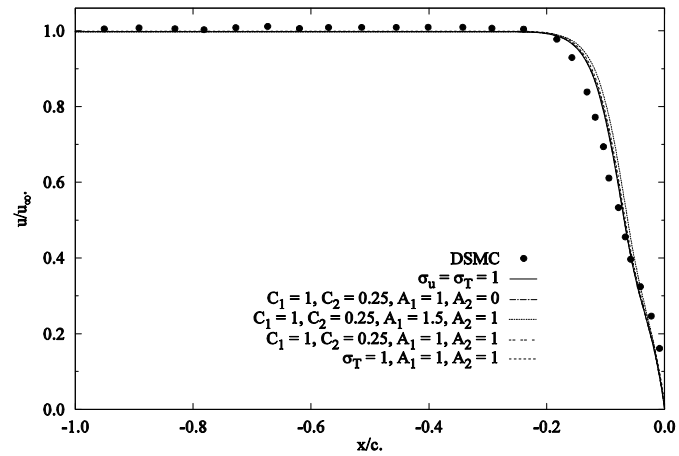

Fig. 5. Slip velocity distribution along the stagnation line, $M = 2$, AOA = 0-deg, Kn = 0.026.

line, there are slight differences between the CFD results using the first order and the second order conditions for pressure, temperature, and velocity, seen in Figs. 3, 4 and 5. There is an increase of gradient-length local Knudsen number, $Kn_{GLL} = \lambda|\nabla\rho|/\rho$, based on the density gradient at the core of the bow shock and near the leading edge of the airfoil, $-0.2 < x/c < 0$, seen in Fig. 3. The Kn_{GLL} of all CFD results are almost the same; therefore, only the Kn_{GLL} of the second order conditions with $A_1 = 1$, $A_2 = 1$, $C_1 = 1$, $C_2 = 0.25$ is presented in Fig. 3 to show the rarefaction effects along the stagnation line. The Kn_{GLL} increases to peak value of 0.25 and then quickly decreases to zero value at the location $x/c = -0.2$. Comparison between DSMC and CFD results for shock wave and rarefied gas flows in [35] showed that the N-S-F equations are inappropriate wherever Kn_{GLL} exceeds 0.05. The pressure and temperature are initially constant at their free stream values before increasing as the flow is compressed in the bow shock region. There are differences between DSMC data [8] and all CFD results at the front of the leading edge of the airfoil because the Kn_{GLL} exceeds 0.05 in the core of the bow shock region, $-0.2 \le x/c \le -0.05$, as seen in Figs. 3 and 4. On the other hand, the velocity is initially constant at the free stream value before decreasing in the bow shock region. There are also differences between the CFD results and DSMC data for slip velocity in the range $-0.2 \le x/c \le -0.05$, as shown in Fig. 5.

Fig. 6 compares the surface pressure coefficient distribution, C_p, along the airfoil surface between all CFD results and DSMC data. There is a suitable agreement between all CFD results and DSMC data. The CFD method predicts lower C_p than DSMC data. This is caused by the rarefaction effects (the increase of Kn_{GLL}) in the region adjacent to the airfoil surface in the range $0.05 \le x/c \le 0.35$. There is a slight difference between the CFD results predicted by the second order conditions when increasing A_1 or A_2.

Fig. 7 presents the surface gas temperature along the airfoil surface. The second order conditions with $A_1 = 1$, $A_2 = 0$, $C_1 = 1$, $C_2 = 0.25$ predicts the highest temperatures, and they are close to DSMC data [8]. We provided the comparison of DSMC solutions for both translational and overall temperatures. It should be noted that due to the low incoming static/stagnation temperatures; the translational and rotational temperatures are almost equal. It means

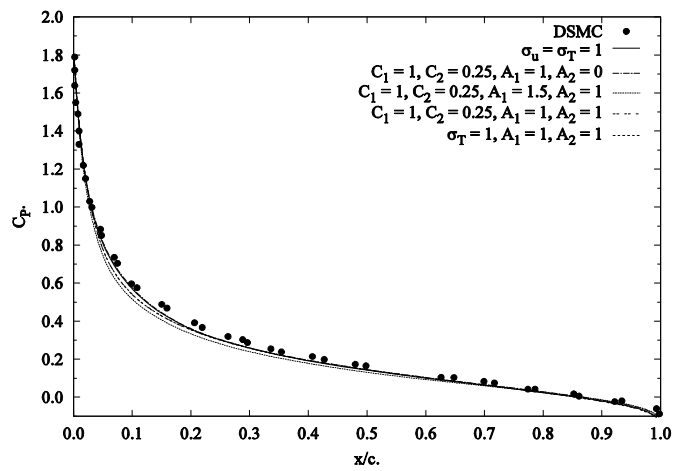

Fig. 6. Surface pressure coefficient, C_P, distribution along the airfoil surface, $M = 2$, AOA = 0-deg, Kn = 0.026.

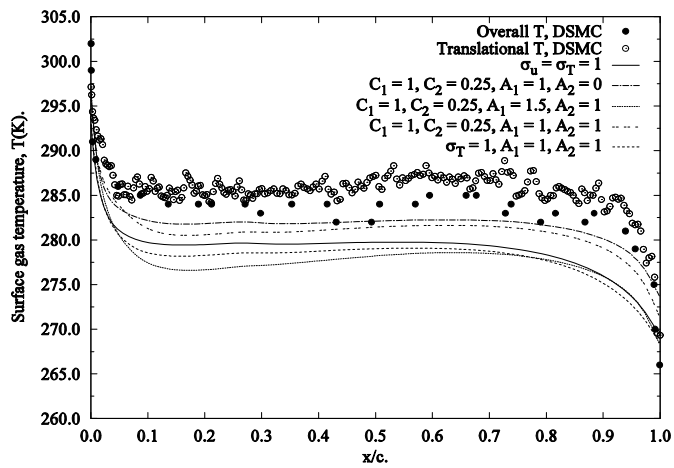

Fig. 7. Surface gas temperature distribution along the airfoil surface, $M = 2$, AOA = 0-deg, Kn = 0.026.

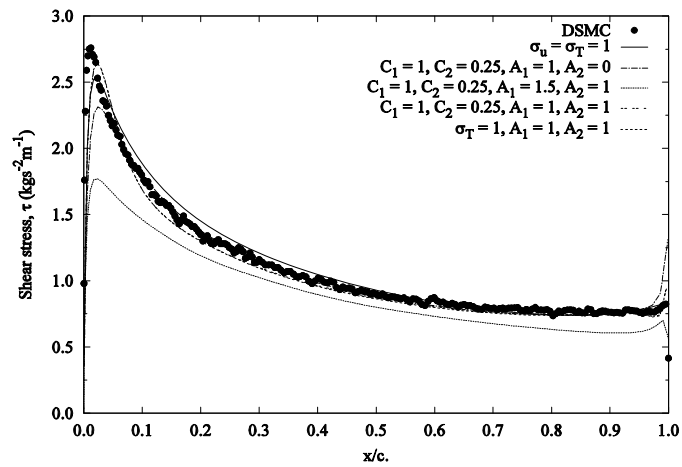

Fig. 8. Shear stress distribution along the airfoil surface, $M = 2$, AOA = 0-deg, Kn = 0.026.

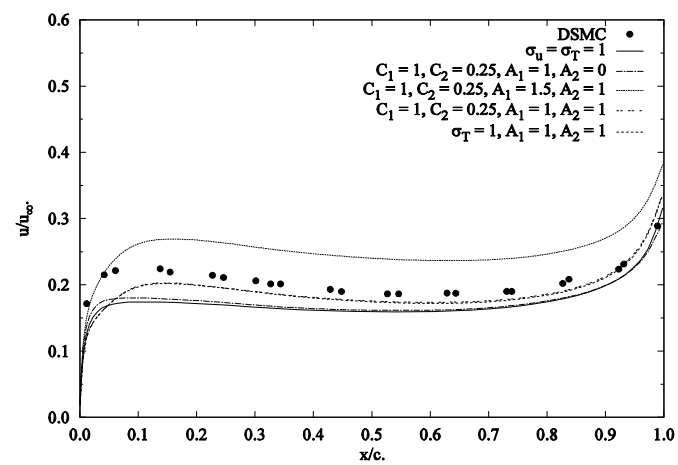

Fig. 9. Slip velocity distribution along the airfoil surface, $M = 2$, AOA = 0-deg, Kn = 0.026.

the conventional NSF equations are accurate enough to describe the flow, and there is no need for a further addition of governing equations for rotational energies. The simulation results of the second order conditions with $A_1 = 1.5$, $A_2 = 1$, $C_1 = 1$, $C_2 = 0.25$ are the lowest ones compared with those of the first order conditions and the second order conditions with $A_1 = 1$, $A_2 = 1$, $C_1 = 1$, $C_2 = 0.25$. For slight rarefied gas flows such as Kn = 0.026, the increased velocity near the surface will cause a reduction of the heat transfer [36]. As expected, the surface gas temperatures decrease when increasing A_1 from 1 to 1.5 or A_2 from 0 to 1. This decrease is observed in comparison between the simulation results of the case $A_1 = 1$, $A_2 = 1$, $C_1 = 1$, $C_2 = 0.25$ with the cases $A_1 = 1$, $A_2 = 0$, $C_1 = 1$, $C_2 = 0.25$ and $A_1 = 1.5$, $A_2 = 1$, $C_1 = 1$, $C_2 = 0.25$. Comparing the simulation results of the first order conditions, $\sigma_u = \sigma_T = 1$ (equal to $A_1 = 1$, $A_2 = 0$, $C_1 = 1$, $C_2 = 0$), with those of the second order conditions $A_1 = 1$, $A_2 = 0$, $C_1 = 1$, $C_2 = 0.25$ and $\sigma_T = 1$, $A_1 = 1$, $A_2 = 1$, the simulation results show that surface gas temperatures increase and decrease when the C_2 and A_2 increases, respectively.

Fig. 8 presents the shear stresses of the CFD and DSMC results. The shear stress reaches the peak values at near the tip of the airfoil as follows: 2.561 for the first order condition case, 2.365 for the case $A_1 = 1$, $A_2 = 0$, $C_1 = 1$, $C_2 = 0.25$, 2.687 for the case $A_1 = 1$, $A_2 = 1$, $C_1 = 1$, $C_2 = 0.25$, 1.79 for the case $A_1 = 1.5$, $A_2 = 1$, $C_1 = 1$, $C_2 = 0.25$, and 2.684 for the cases $\sigma_T = 1$, $A_1 = 1$, $A_2 = 1$. Past these peak points, they gradually decrease along the airfoil the surface. All CFD simulation results give good agreement with DSMC data, except the CFD one with $A_1 = 1.5$, $A_2 = 1.0$, $C_1 = 1$ and $C_2 = 0.25$. The CFD simulations show that the increase of A_1 or A_2 will decrease the shear stress at AOA = 0-deg. Fig. 9 shows the normalized slip velocity distribution along the airfoil surface. The increase of A_1 or A_2, i.e. adding more normal velocity gradient, will make an increase of the slip velocity. The slip velocity predicted by the second order conditions with $A_1 = 1.5$, $A_2 = 1$, $C_1 = 1$, $C_2 = 0.25$ are the highest one. The CFD results of the first order conditions with $\sigma_u = 1$ (equal to $A_1 = 1$, $A_2 = 0$) are the lowest ones. The CFD results of the second order slip condition with $A_1 = 1$, $A_2 = 1$, $C_1 = 1$, $C_2 = 0.25$ show a reasonable agreement with DSMC data.

6.2. *NACA 0012 airfoil case* $M = 2$, Kn = 0.026, *AOA* = 10-*deg*

The CFD simulations using the second order conditions are also run for four cases with various coefficients as follows 1) $A_1 = 1$, $A_2 = 0$, $C_1 = 1$, $C_2 = 0.25$, 2) $A_1 = 1$, $A_2 = 1$, $C_1 = 1$, $C_2 = 0.25$, 3) $A_1 = 1.5$, $A_2 = 1$, $C_1 = 1$, $C_2 = 0.25$, and 4) $\sigma_T = 1$, $A_1 = 1$, $A_2 = 1$. As AOA = 10°, Figs. 10a and 10b compare the pressure coefficient distribution, C_P, over the lower and upper airfoil surfaces. The C_P reaches the peak values at the tip of the lower and upper surfaces. Past these peak locations, the C_P gradually decreases along the both of airfoil surfaces. Overall, there is a good agreement between DSMC data [8] and all CFD results. The pressures expressed via the C_P over the lower surface are greater than those

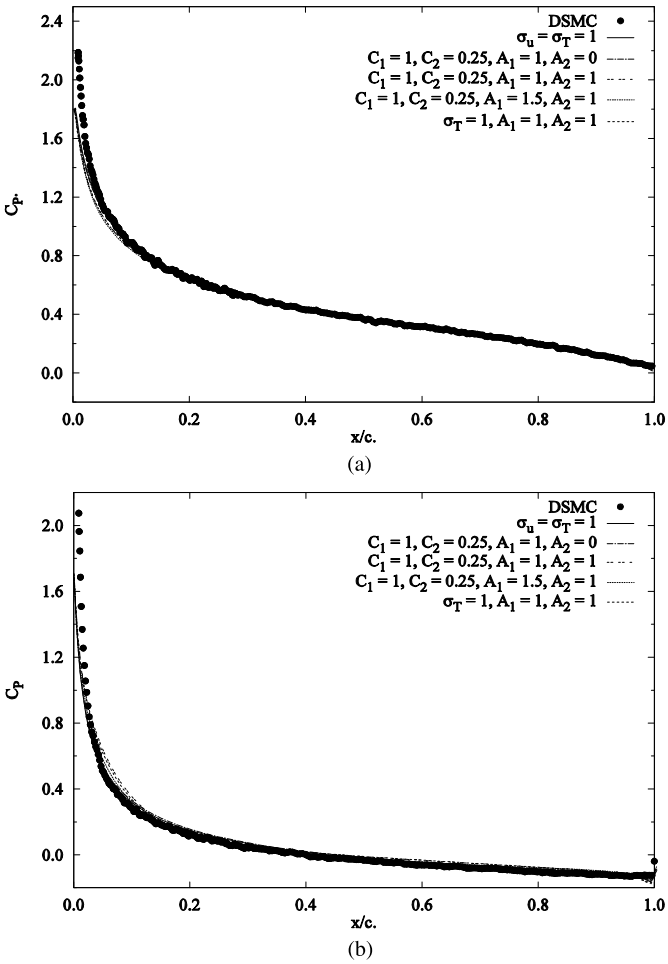

Fig. 10. (a) Surface pressure coefficient, C_P, distribution along the lower surface, $M = 2$, AOA = 10-deg, Kn = 0.026. (b) Surface pressure coefficient, C_P, distribution along the upper surface, $M = 2$, AOA = 10-deg, Kn = 0.026.

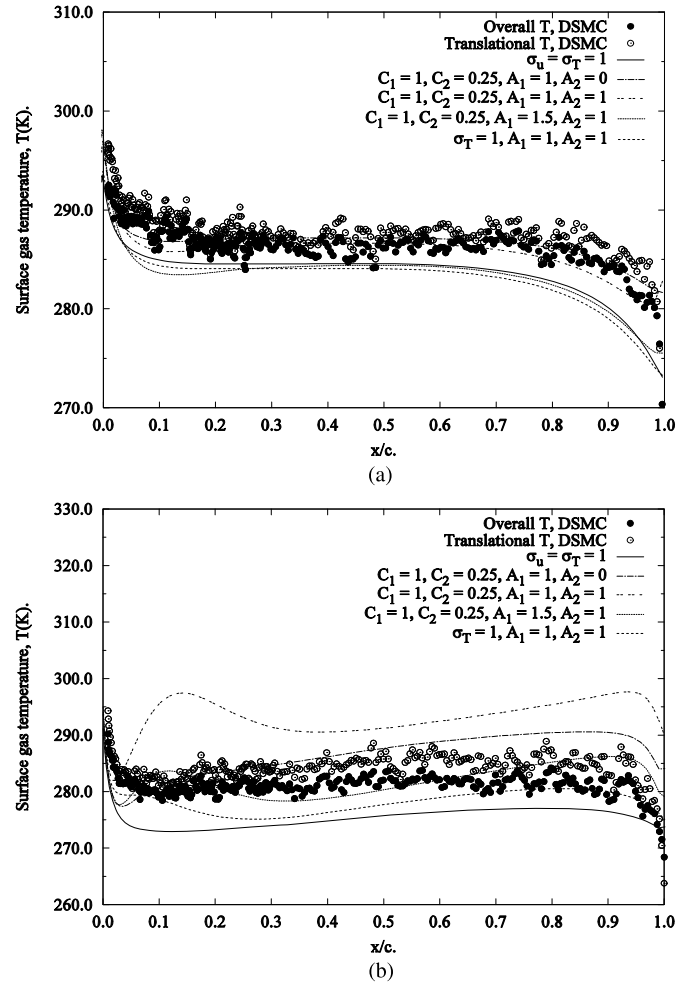

Fig. 11. (a) Surface gas temperature distribution along the lower surface, $M = 2$, AOA = 10-deg, Kn = 0.026. (b) Surface gas temperature distribution along the upper surface, $M = 2$, AOA = 10-deg, Kn = 0.026.

over the upper surface. This causes a lift force to push the airfoil upward, normal to the incoming flow stream.

Figs. 11a and 11b compare the surface gas temperatures between the lower and upper surfaces. In comparison, the simulation results between the cases $A_1 = 1.5$, $A_2 = 1$ and $A_1 = 1$, $A_2 = 1$, the increase of A_1 results in the reduction of surface gas temperature for both surfaces. Both translational and overall temperatures are almost the same in the DSMC. The simulation results of the second order conditions with $A_1 = 1$, $A_2 = 0$, $C_1 = 1$, $C_2 = 0.25$ and $A_1 = 1$, $A_2 = 1$, $C_1 = 1$, $C_2 = 0.25$ point out that the increase of A_2 decreases the surface gas temperatures over the lower surface and increases those over the upper surface. The CFD results over the lower surface using the second order conditions with $A_1 = 1$, $A_2 = 0$, $C_1 = 1$, $C_2 = 0.25$, and $A_1 = 1$, $A_2 = 1$, $C_1 = 1$, $C_2 = 0.25$ give a suitable agreement with DSMC data [8], while those using the second order conditions with $A_1 = 1.5$, $A_2 = 1$, $C_1 = 1$, $C_2 = 0.25$ give a suitable agreement with DSMC data over the upper surface. The simulation with the first order conditions underpredicts the surface gas temperature for both surfaces. The simulation results of the case $A_1 = 1$, $A_2 = 0$, $C_1 = 1$, $C_2 = 0.25$ and the case $\sigma_u = \sigma_T = 1$ (equal to $A_1 = 1$, $A_2 = 0$, $C_1 = 1$, $C_2 = 0$) show that the surface gas temperatures increase when the C_2 increases. The results of the cases $\sigma_u = \sigma_T = 1$ and $\sigma_T = 1$, $A_1 = 1$, $A_2 = 1$ point out that the increase of A_2 will decrease the temperature over the lower surface and increase over the upper surface.

Figs. 12a and 12b present the shear stresses over the upper and lower surfaces. The shear stress reaches the peak values at near the tip of the airfoil. Past the peak values, they gradually decrease along the airfoil surface. The simulation results over the lower surface with the cases $A_1 = 1$, $A_2 = 0$, $C_1 = 1$, $C_2 = 0.25$ and $\sigma_u = \sigma_T = 1$ give the best agreement with DSMC data. The shear stresses over the upper surface of the cases with $A_1 = 1$, $A_2 = 1$, $C_1 = 1$, $C_2 = 0.25$, and $\sigma_T = 1$, $A_1 = 1$, $A_2 = 1$ give a better agreement with DSMC data. Corresponding to the shear stress distribution for $x/c < 0.04$, the normalized slip velocities are slow due to the viscous stresses, as seen in Figs. 13a and 13b. For $x/c \geq 0.04$, all CFD results and DSMC data [8] are nearly constant values over the lower surface towards the location $x/c = 0.65$ and thereafter gradually increase to trailing edge of the airfoil. In comparison, between the CFD results of the second order conditions, the increase of A_1 or A_2 results in the rise of the slip velocities over the lower surface. It is observed that the slip velocity predicted by the second order slip conditions with the $A_1 = 1.5$, $A_2 = 1$, and the $A_1 = 1$, $A_2 = 1$ oscillates along the upper surface while that using the first order slip condition does not. This illustrates, there is a numerical difficulty associated with accurate calculations of the second order derivative of the velocity gradient normal to the curved surface due to increasing AOA, in particular, the upper surface. This may explain the decrease of the slip velocity over the upper surface when the A_2 increases, as seen the results of the cases $A_1 = 1$, $A_2 = 0$ and $A_1 = 1$, $A_2 = 1$ in Fig. 10b. The increase of A_1 also results in the slip velocity increases on the upper surface. On the lower surface, the simulation results using the second

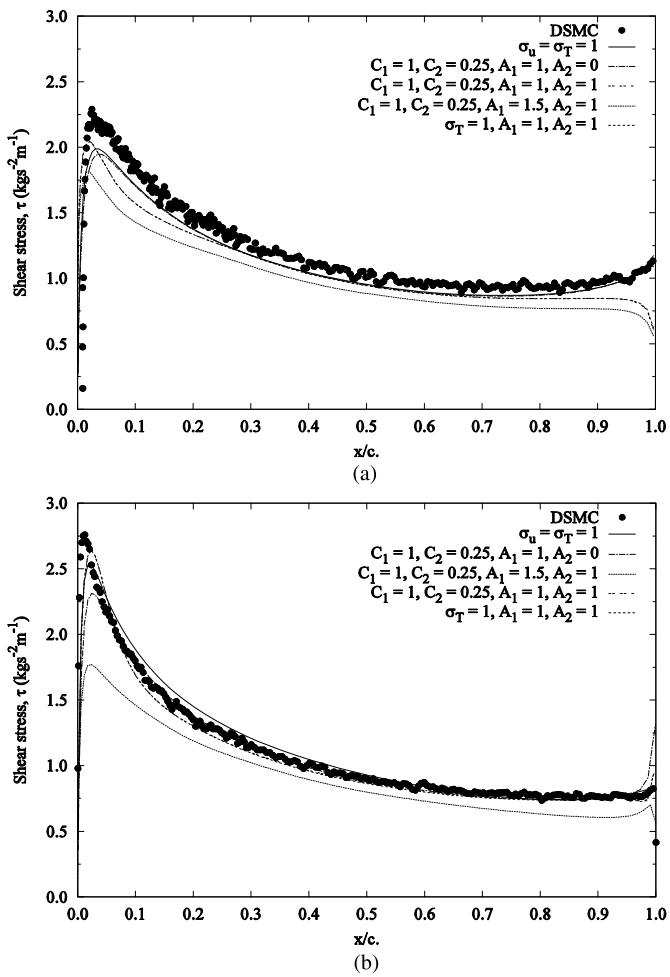

Fig. 12. (a) Shear stress distribution along the lower surface, $M = 2$, AOA = 10-deg, Kn = 0.026. (b) Shear stress distribution along the upper surface, $M = 2$, AOA = 10-deg, Kn = 0.026.

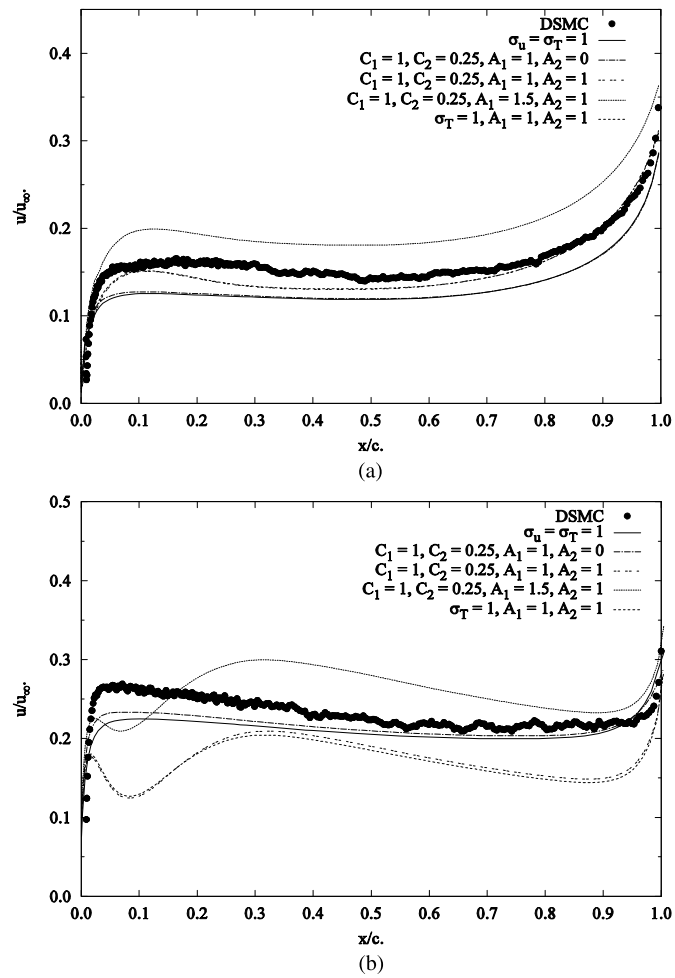

Fig. 13. (a) Slip velocity distribution along the lower surface, $M = 2$, AOA = 10-deg, Kn = 0.026. (b) Slip velocity distribution along the upper surface, $M = 2$, AOA = 10-deg, Kn = 0.026.

order conditions with $A_1 = 1$, $A_2 = 1$, $C_1 = 1$, $C_2 = 0.25$ give good agreement with DSMC data. The slip velocity predicted by the second order conditions with $A_1 = 1$, $A_2 = 0$, $C_1 = 1$, $C_2 = 0.25$ give a relatively suitable agreement with DSMC data over the upper surface. Comparing the results between the cases $A_1 = 1$, $A_2 = 0$, $C_1 = 1$, $C_2 = 0.25$ and $\sigma_u = \sigma_T = 1$ (equal to $A_1 = 1$, $A_2 = 0$, $C_1 = 1$, $C_2 = 0$), the slip velocity slightly increases if C_2 increases.

For completeness, the normalized density contours (ρ/ρ_∞) of the CFD simulations are compared with experimental data, seen in Figs. 14a, 14b and 14c. There is a relative agreement between the CFD results and experimental data [4,7] for the slight rarefied gas at Kn = 0.026.

6.3. NACA 0012 airfoil case $M = 0.8$, Kn = 0.014, AOA = 0-deg

Three CFD simulations are run with the first order conditions and the second order conditions with $A_1 = 1$, $A_2 = 1$, $C_1 = 1$, $C_2 = 0.25$, $A_1 = 1$, $A_2 = 0.5$, $C_1 = 1$, $C_2 = 0.2$, and $\sigma_T = 1$, $A_1 = 1$, $A_2 = 0.5$. In this case, the rarefied air flow at the subsonic ($M = 0.8$) is investigated around the airfoil with the AOA = 0°. Unlike the supersonic case there is no the bow shock in the subsonic case. The pressure is lower than that of free stream upon most of the airfoil surface (presented by the negative C_P in the range $0.165 \le x/c \le 1$) that is caused by the increase of viscous effect, as seen in Fig. 15. The C_p reaches the peak values at the tip of the airfoil. Past the tip location, the C_p gradually decreases towards the location $x/c = 0.6$ and holds a nearly constant value in the range $0.6 \le x/c \le 1$. The C_p coefficients of the CFD results are lower than the DSMC data [8] due to the rarefaction effects at near the leading edge of the airfoil. Overall, there is reasonable agreement between the DSMC data and all CFD results.

As seen in Fig. 16, the surface gas temperatures reach the peak values at the tip of the airfoil. Past the tip location, the temperatures gradually decrease towards the location, $x/c = 0.08$ and then increases slightly along the airfoil surface. Both translational and overall temperatures are almost the same. The CFD results using the first order conditions and the second order conditions with $A_1 = 1$, $A_2 = 0.5$, $C_1 = 1$, $C_2 = 0.2$ are close to DSMC data [8]. Comparing the results with the $\sigma_u = \sigma_T = 1$ and $\sigma_T = 1$, $A_1 = 1$, $A_2 = 0.5$, it is seen that the temperature decreases as A_2 increase.

Fig. 17 compares the DSMC and CFD shear stresses. They reach the peak values at near the tip of the airfoil as follows: 2.067 for DSMC, 1.67 for the case $\sigma_u = \sigma_T = 1.0$, 1.6972 for the case $A_1 = 1$, $A_2 = 1$, $C_1 = 1$, $C_2 = 0.25$, 1.7855 for the case $A_1 = 1$, $A_2 = 1$, $C_1 = 1$, $C_2 = 0.25$, and 1.6979 for the case $\sigma_T = 1.0$, $A_1 = 1$, $A_2 = 0.5$. Past the peak values, they gradually decrease along the airfoil surface. It is unlike the supersonic case at the AOA of 0-deg, the increase of A_1 or A_2 will increase the peak values of the shear stresses. In the range, $0.1 < x/c < 0.4$, the simulation results with $\sigma_u = \sigma_T = 1.0$ are relatively close to DSMC data. Beyond this range the CFD results with $A_1 = A_2 = 1.0$, $C_1 = 1$, $C_2 = 0.2$ give the best agreement with DSMC data. For the CFD results, the normalized slip velocity predicted by the second order condition with $A_1 = 1$, $A_2 = 1$, $C_1 = 1$, $C_2 = 0.25$ is the highest while that predicted

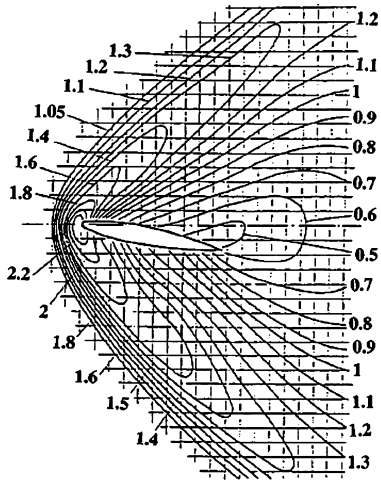

(a) Experiment

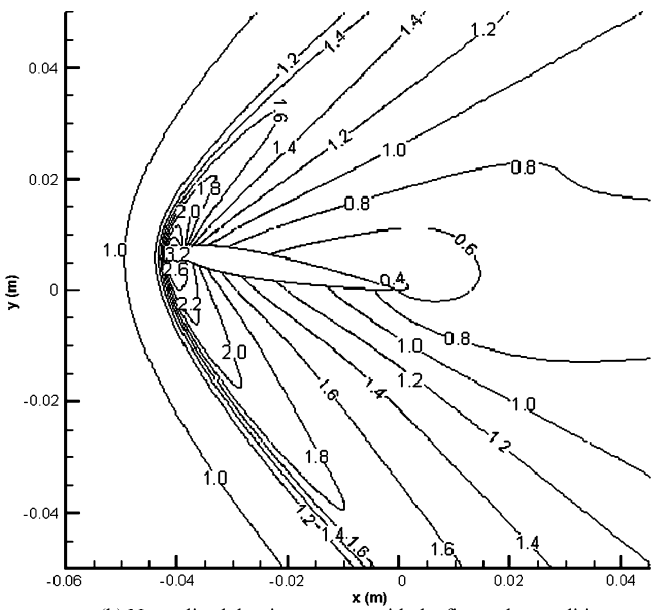

(b) Normalized density contours with the first order conditions

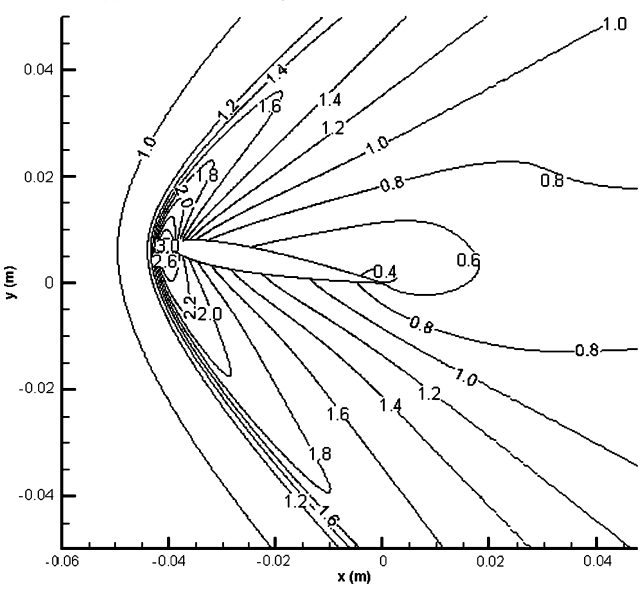

(c) Normalized density contours with the second order conditions

Fig. 14. Normalized density contours (ρ/ρ_∞) of the case $M = 2$, AOA = 10-deg, Kn = 0.026 (a) experiment [4], (b) first order conditions, and (c) second order conditions, $A_1 = 1$, $A_2 = 1$, $C_1 = 1$, $C_2 = 0.25$.

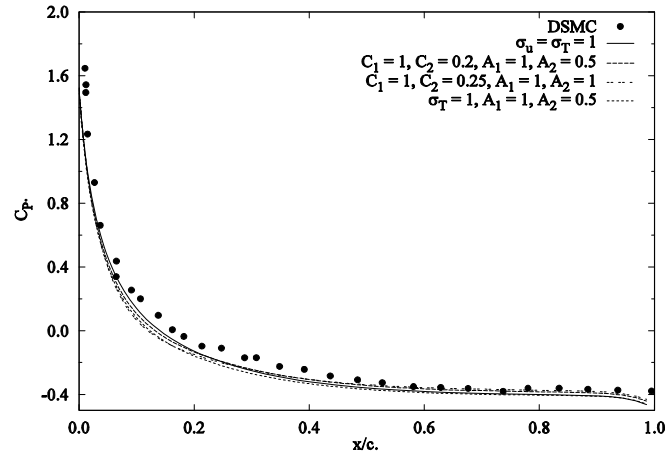

Fig. 15. Surface pressure coefficient, C_P, distribution along the airfoil surface, $M = 0.8$, AOA = 0-deg, Kn = 0.014.

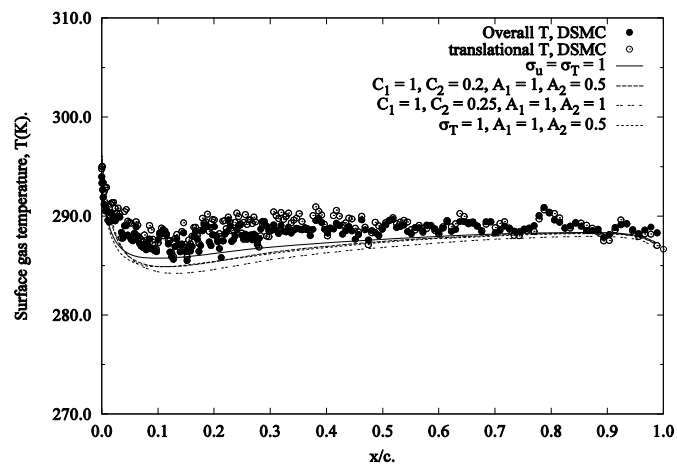

Fig. 16. Surface gas temperature distribution along the airfoil surface, $M = 0.8$, AOA = 0-deg, Kn = 0.014.

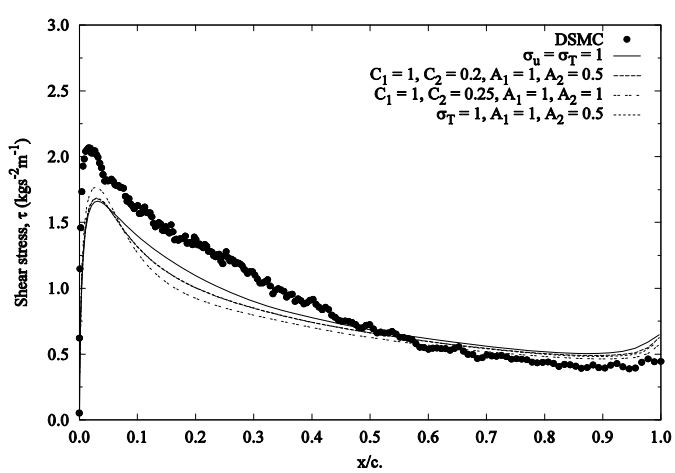

Fig. 17. Shear stress distribution along the airfoil surface, $M = 0.8$, AOA = 0-deg, Kn = 0.026.

by the first order condition is the lowest, as seen in Fig. 18. The CFD results use the second order conditions with $A_1 = 1$, $A_2 = 0.5$, $C_1 = 1$, $C_2 = 0.2$ are close to DSMC data [8] for $x < 0.4$ and those using the first order conditions are close to DSMC data for $x \geq 0.4$.

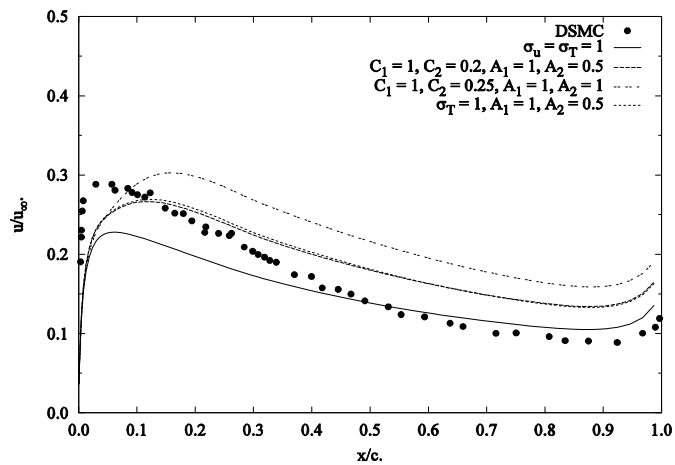

Fig. 18. Slip velocity along distribution along the airfoil surface, $M = 0.8$, AOA = 0-deg, Kn = 0.014.

6.4. Lift and drag coefficients of the NACA 0012 airfoil case $M = 2$, Kn = 0.026 at various AOAs

The lift, C_L, and drag, C_D, coefficients of the supersonic airfoil case, $M = 2$, Kn = 0.026 are computed at different AOAs and compared with DSMC data [8]. The C_L and C_D coefficients are calculated in OpenFOAM as follows:

$$C_L = \frac{F_L}{0.5\rho_\infty \mathbf{u}_\infty^2 A_{ref}}, \tag{16}$$

$$C_D = \frac{F_D}{0.5\rho_\infty \mathbf{u}_\infty^2 A_{ref}}, \tag{17}$$

where F_L and F_D are the lift and drag forces, and A_{ref} is computed by the product of a cell length of two-dimensional mesh in the direction of axis z (span of airfoil) and the length of the chord, $A_{ref} = 0.0086$ m. At each AOA, five simulations are run with the first order conditions and the second order conditions with 1) $\sigma_u = \sigma_T = 1$; 2) $A_1 = 1.5$, $A_2 = 1$, $C_1 = 1$, $C_2 = 0.25$; 3) $A_1 = 1$, $A_2 = 1$, $C_1 = 1$, $C_2 = 0.25$; 4) $A_1 = 1$, $A_2 = 0.25$, $C_1 = 1$, $C_2 = 0.2$; and 5) $\sigma_T = 1$, $A_1 = 1$, $A_2 = 1$. Five AOAs are investigated as 0, 5, 10, 15 and 20-deg. Tables 2 and 3 compare the drag and lift coefficients of the CFD and DSMC calculations, respectively. The values C_D and C_L increase with the increase of AOA. They have minimum values at the AOA = 0-deg for C_D and AOA = 5-deg for C_L, and maximum values at AOA = 20-deg. The average errors of the C_D and C_L between the DSMC data and CFD results are also shown in Tables 2 and 3. For the C_D, the case with $A_1 = 1$, $A_2 = 1$, $C_1 = 1$, $C_2 = 0.25$ gives the smallest average error of 0.412% compared with the DSMC data. For the C_L, the case with $\sigma_u = \sigma_T = 1$ the smallest average error of 0.264% compared with DSMC data. The cases with $A_1 = 1.5$, $A_2 = 1$, $C_1 = 1$, $C_2 = 0.25$ and $A_1 = 1$, $A_2 = 1$, $C_1 = 1$, $C_2 = 0.25$ give the average error of 2.564% and 1.1052%, respectively. The results figure out that the increase of A_1 will decrease the average error of C_L.

6.5. Discussions on second order slip/jump BC's coefficients

Here, we summarize the best values of coefficients of the second order boundary conditions for predicting surface quantities such as: shear stress, temperature jump and slip velocity, and drag coefficients of the airfoil cases in comparing with DSMC data, see Table 4.

It should be noted that the coefficients of the second order slip condition were suggested by many researchers differently, i.e., in [37–42], they were proposed either from theoretical considerations or inferred from experimental observations. Their values are still the subject of much discussion. It should be mentioned that the variation of the coefficients of the second order conditions does not mean the change of the accommodation coefficients, but it is a numerical approach to finding the correct solution. In this work, we numerically adjusted these coefficients to match DSMC data. The simulation results figure out this numerical approach is suitable to obtain a good agreement with the correct solution, in particular, the DSMC method. It should be mentioned that the change of the coefficients values is limited to a narrow range.

6.6. Heat flux distribution over the airfoil surfaces

The heat transfers to the airfoil surface of all cases are shown in Figs. 19a, 19b, 19c and 19d. For the cases supersonic, $M = 2$, all CFD simulations with either the first order conditions or the second order conditions do not give good agreement with DSMC data, seen Figs. 19a, 19b and 19c. For the subsonic case $M = 0.8$, there is a relative agreement between the CFD and DSMC results, as seen in Fig. 19d. This can be explained by the different nature of the computation between DSMC and CFD method as shown in Eq. (13) for DSMC and the Fourier law $\mathbf{Q} = -k\nabla T$ for CFD. The contribution of the velocity terms in Eq. (13) such as thermal velocity and molecular velocity results in the heat transfer of DSMC to be positive at near the tip of the airfoil, while those of CFD are negative due to the temperature gradient only. These velocity terms also

Table 2
The average errors of the drag coefficient between the DSMC data and CFD results.

	0-deg	5-deg	10-deg	15-deg	20-deg	Average error (%)
$\sigma_u = \sigma_T = 1$	0.3999	0.4107	0.4533	0.5223	0.6133	**0.834**
$A_1 = 1$, $A_2 = 1$, $C_1 = 1$, $C_2 = 0.25$	0.3915	0.4066	0.4583	0.5286	0.6336	**0.412**
$A_1 = 1.5$, $A_2 = 1$, $C_1 = 1$, $C_2 = 0.25$	0.3654	0.3824	0.4322	0.5035	0.6086	**2.942**
$A_1 = 1$, $A_2 = 0.5$, $C_1 = 1$, $C_2 = 0.2$	0.3951	0.4077	0.4555	0.5250	0.6225	**0.668**
$A_1 = 1$, $A_2 = 1$, $\sigma_T = 1$	0.3912	0.4062	0.4573	0.5276	0.6323	**0.4885**
DSMC	0.4109	0.4210	0.4609	0.5270	0.6194	

Table 3
The average errors of the lift coefficient between the DSMC data and CFD results.

	5-deg	10-deg	15-deg	20-deg	Average error (%)
$\sigma_u = \sigma_T = 1$	0.1758	0.3511	0.5201	0.6757	**0.264**
$A_1 = 1$, $A_2 = 1$, $C_1 = 1$, $C_2 = 0.25$	0.1705	0.3294	0.4924	0.6135	**2.566**
$A_1 = 1.5$, $A_2 = 1$, $C_1 = 1$, $C_2 = 0.25$	0.1777	0.3444	0.5156	0.6429	**1.105**
$A_1 = 1$, $A_2 = 0.5$, $C_1 = 1$, $C_2 = 0.2$	0.1728	0.3394	0.5049	0.6384	**1.608**
$A_1 = 1$, $A_2 = 1$, $\sigma_T = 1$	0.1716	0.3349	0.4976	0.6206	**2.223**
DSMC	0.1850	0.3523	0.5230	0.6756	

Table 4
Suggested values of coefficients of the second order conditions in predicting surface quantities and drag coefficients for the NACA 0012 airfoil.

Cases	Surface gas temperature	Shear stress	Slip velocity
$M = 0.8$, AOA = 0-deg	$A_1 = 1$, $A_2 = 0.5$, $C_1 = 1$, $C_2 = 0.2$.	$A_1 = 1$, $A_2 = 1$, $C_1 = 1$, $C_2 = 0.2$.	$A_1 = 1$, $A_2 = 0.5$, $C_1 = 1$, $C_2 = 0.2$.
$M = 2$, AOA = 0-deg	$A_1 = 1$, $A_2 = 0$, $C_1 = 1$, $C_2 = 0.25$.	$A_1 = 1$, $A_2 = 1$, $C_1 = 1$, $C_2 = 0.25$.	$A_1 = 1$, $A_2 = 1$, $C_1 = 1$, $C_2 = 0.25$.
$M = 2$, AOA = 0-deg, lower airfoil surface	$A_1 = 1$, $A_2 = 1$, $C_1 = 1$, $C_2 = 0.25$.	$A_1 = 1$, $A_2 = 0$, $C_1 = 1$, $C_2 = 0.25$.	$A_1 = 1$, $A_2 = 1$, $C_1 = 1$, $C_2 = 0.25$.
$M = 2$, AOA = 0-deg, upper airfoil surface	$A_1 = 1.5$, $A_2 = 1$, $C_1 = 1$, $C_2 = 0.25$.	$A_1 = 1$, $A_2 = 1$, $C_1 = 1$, $C_2 = 0.25$.	$A_1 = 1$, $A_2 = 0$, $C_1 = 1$, $C_2 = 0.25$.
Drag coefficients		$A_1 = 1$, $A_2 = 1$, $C_1 = 1$, $C_2 = 0.25$	

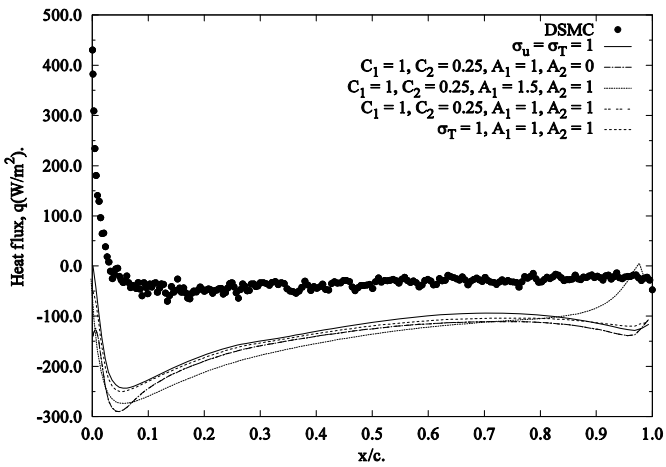

(a) M = 2, AOA = 0-deg, Kn = 0.026

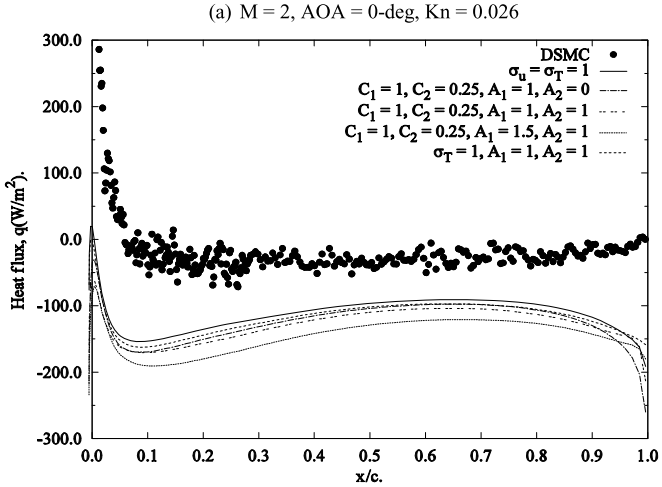

(b) the upper surface M = 2, AOA = 10-deg, Kn = 0.026.

Fig. 19. Heat flux distribution over the airfoil surfaces (a) $M = 2$, AOA = 0-deg, Kn = 0.026, (b) the upper surface $M = 2$, AOA = 10-deg, Kn = 0.026, (c) the lower surface $M = 2$, AOA = 10-deg, Kn = 0.026, and (d) $M = 0.8$, AOA = 0-deg, Kn = 0.014.

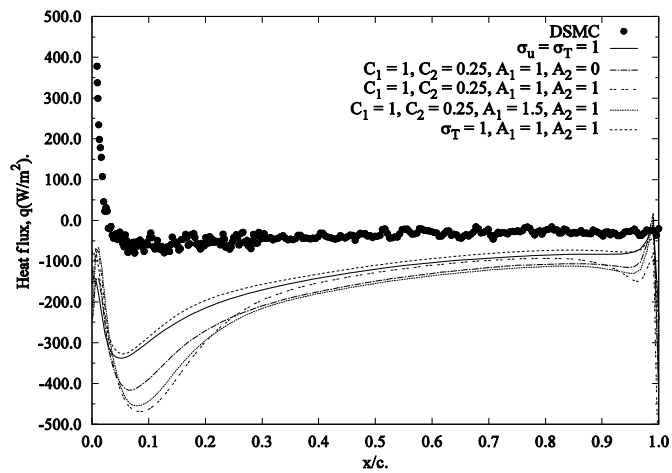

(c) the lower surface M = 2, AOA = 10-deg, Kn = 0.026.

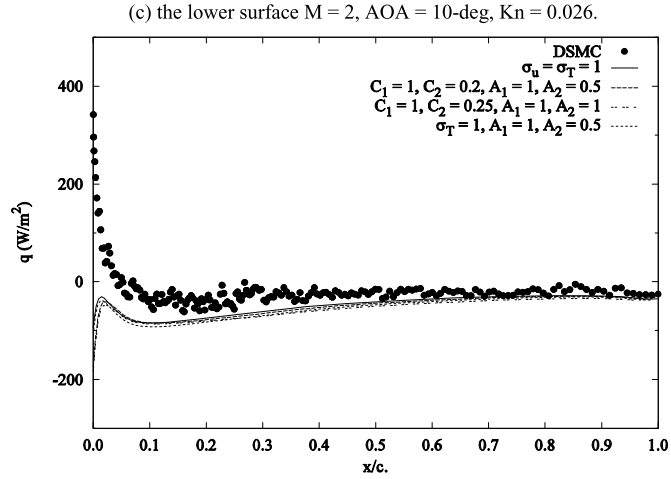

(d) M = 0.8, AOA = 0-deg, Kn = 0.014.

Fig. 19. (*continued*)

lead to a large difference between the DSMC and CFD heat fluxes for the supersonic cases.

6.7. Sharp 25–55-deg biconic case, $M = 15.6$

In this case, the first order conditions, $\sigma_u = \sigma_T = 1$, the case with $A_1 = 1$, $A_2 = 0.5$, $C_1 = 1$, $C_2 = 0.2$, and the case with $\sigma_T = 1$, $A_1 = 1$, $A_2 = 0.5$ are used for the CFD simulations. First of all, the mesh independence is studied with four different meshes: 128×128, 256×128, 256×256, and 512×256 (i.e. 512 cells in the axial, streamwise direction and 256 cells in the radial, surface normal direction). The simulation results of the heat fluxes and the slip velocity predicting by the first order conditions of these meshes are presented in Figs. 20 and 21. The simulation results obtained show that the mesh 256×256 is a fine enough mesh for simulation of the biconic case.

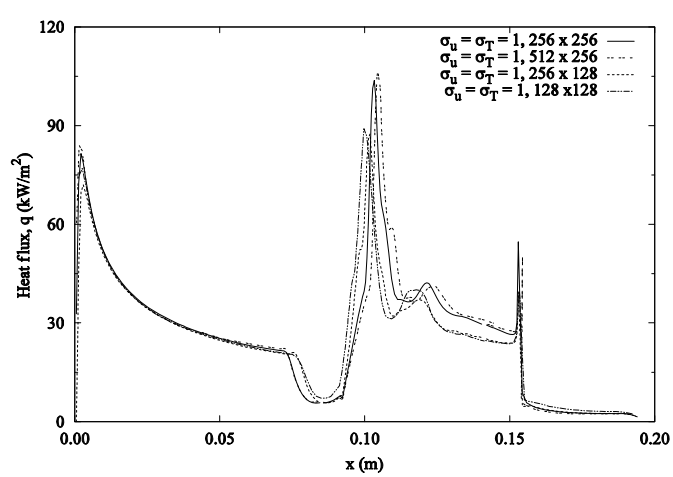

Fig. 20. Heat flux distribution over the biconic surface with various mesh sizes.

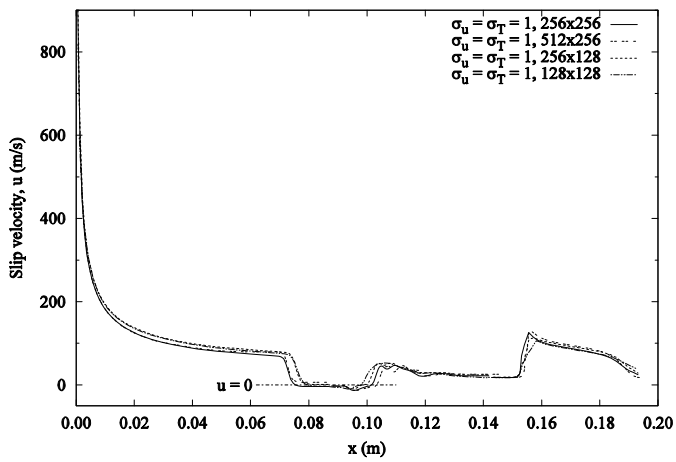

Fig. 21. Slip velocity over the biconic surface with various mesh sizes.

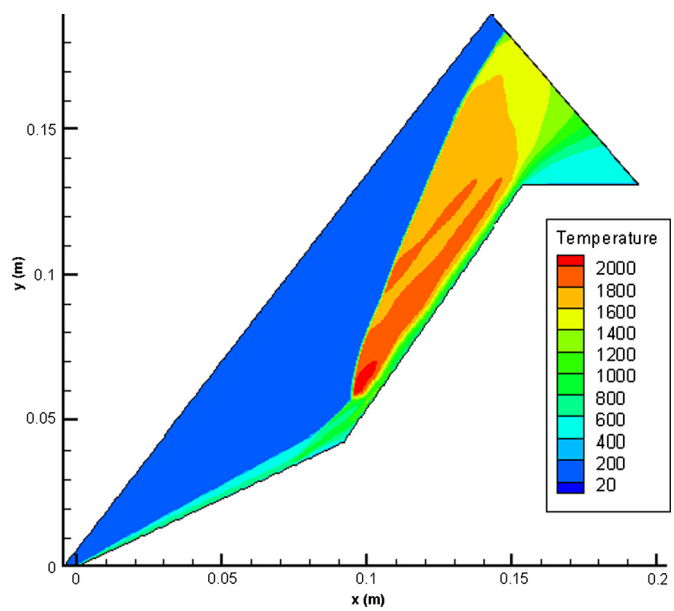

Fig. 22. Temperature field of the biconic case with the second order conditions, $A_1 = 1$, $A_2 = 0.5$, $C_1 = 1$, $C_2 = 0.2$.

Fig. 22 presents the temperature field calculated by the second order conditions with $A_1 = 1$, $A_2 = 0.5$, $C_1 = 1$, $C_2 = 0.2$ for the sharp 25–55-deg biconic case with a maximum temperature, $T_{max} = 2083.65$ K. An oblique shock forms from the tip of the first cone and locates along towards the near the end of this cone, and then separates creating another shock. Latter one interacts with the oblique shock and meets the detached bow shock being formed over the second cone. A low-speed recirculation zone forms at the junction of the first and the second cones in the range $0.0754\ \text{m} \le x \le 0.1021$ m.

Fig. 23 compares the CFD surface pressure distribution along the biconic surface compared with DSMC [19] and experimental [17] data. There is a suitable agreement between all CFD results, DSMC and experimental data of the surface pressures from the tip of the first cone towards location $x = 0.072$ m. Past this point, the flow begins to enter in the area of the recirculation zone, the surface pressures increase to roughly 400 Pa around the location, $x = 0.091$ m, and then continue to gradually increase to reach peak values of 1) 1168.97 Pa at the location $x = 0.1032$ m for the first order conditions, 2) 1147.64 Pa at the location $x = 0.1037$ m for the second order conditions with $A_1 = 1$, $A_2 = 0.5$, $C_1 = 1$, $C_2 = 0.2$, 3) 1158.48 Pa at the location, $x = 0.1037$ for the case with $\sigma_T = 1$, $A_1 = 1$, $A_2 = 0.5$, 4) 1131.72 Pa at the location $x = 0.0985$ m for DSMC, and 5) 1152.74 Pa at the location $x = 0.1$ m for experiment. The interaction of the two shocks produces a high-pressure region that is located on the second cone surface. After reaching the peak values, the surface pressures of the CFD results rapidly drop and oscillate a frequency that is in good agreement with experimental and DSMC data in downstream of the bow shock.

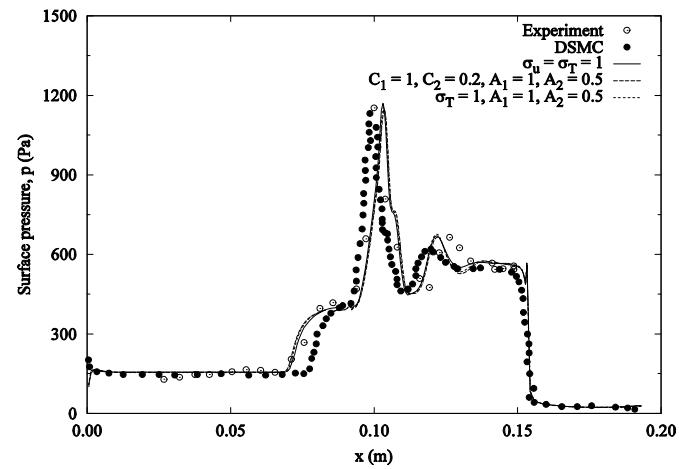

Fig. 23. Surface pressure distribution along the biconic surface.

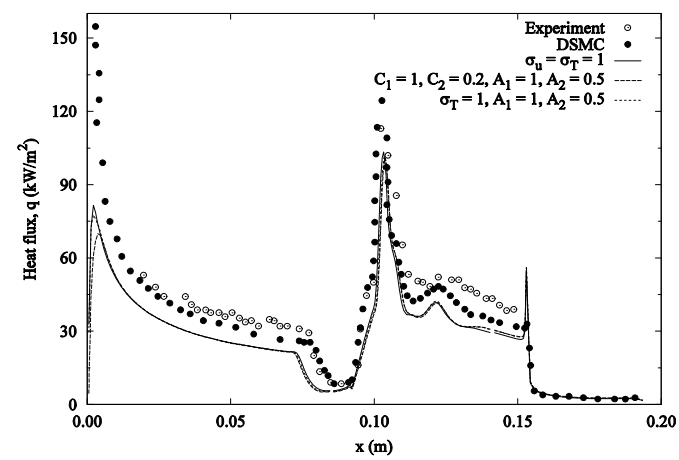

Fig. 24. Heat flux distribution along the biconic surface.

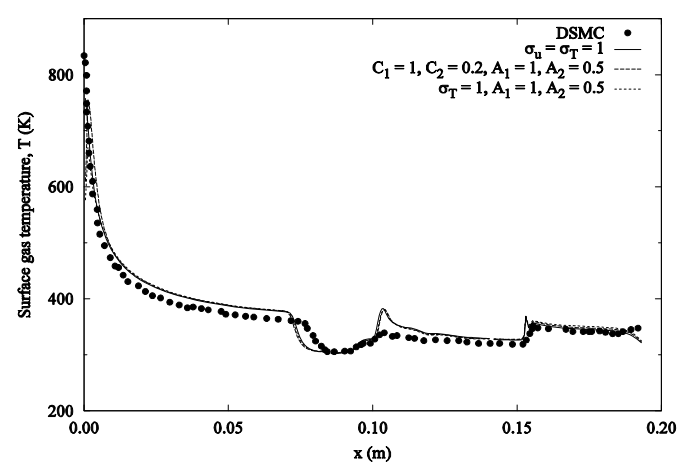

Fig. 25. Surface gas temperature distribution along the biconic surface.

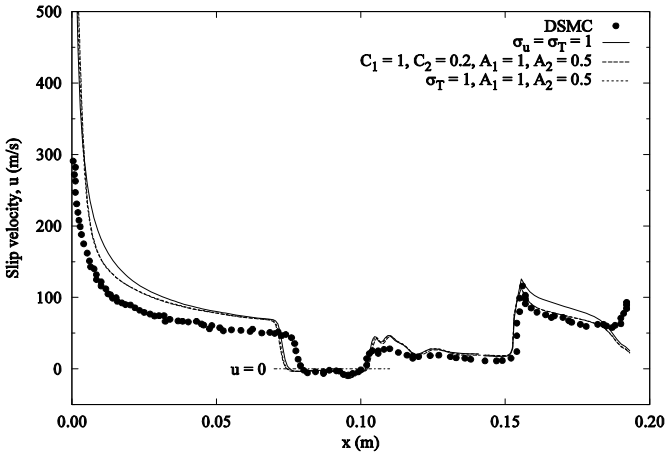

Fig. 26. Slip velocity along the biconic surface.

Fig. 24 compares the CFD heat fluxes with those of DSMC [19] and experiment [17]. Whichever the slip and jump conditions applied on the surface, the CFD underpredicts the heat fluxes along the fore-cone in comparing with DMC and experimental data. There are increases in heat transfer across the recirculation zone. The heat fluxes significantly drop in the range $0.072\ \text{m} \le x \le 0.095\ \text{m}$ within the area of the recirculation zone, and then increase the peak values of 1) 103.59 kW/m^2 at the location $x = 0.1037$ m for the first order conditions $\sigma_u = \sigma_T = 1$, 2) 100.95 kW/m^2 at the location $x = 0.1042$ m for the second order conditions with $A_1 = 1$, $A_2 = 0.5$, $C_1 = 1$, $C_2 = 0.2$, 3) 101.14 kW/m^2 at the location $x = 0.1042$ m for the case $\sigma_T = 1$, $A_1 = 1$, $A_2 = 0.5$, 4) 124.40 kW/m^2 at the location $x = 0.1027$ m for DSMC, and 5) 112.93 kW/m^2 at the location $x = 0.1023$ m experiment in the area of the shock–shock interaction. It is rational that DSMC and NSF solutions disagree on some points due to following reasons, i.e. enhanced nonequilibrium effects that undermine the NSF basic assumptions, i.e., continuum flow field. In this case, even using high order slip and jump conditions could not resolve the issue as these are remedies for moderate departure from the continuum conditions over the surfaces. Past these peak locations, the heat fluxes drop rapidly and oscillate along the second cone. Again the CFD results are lower DSMC and experimental data than along this cone surface ($0.105\ \text{m} \le x \le 0.153$ m). On the base surface, ($0.153\ \text{m} \le x \le 0.192$ m), there is good agreement between all CFD results, DSMC and experiments. Overall, the DSMC method predicts better the heat flux than the CFD method in comparison with the experiment. Fig. 25 shows the surface gas translational temperature between the CFD results and DSMC data. There is a suitable agreement between the CFD results and DSMC data [19] for surface gas temperatures.

Fig. 26 compares the CFD and DSMC [19] slip velocities along the biconic surface. Slip velocities on the biconic surface consist of negative and positive components. Negative ones represent the recirculation zone, and the distance, where indicates the negative slip velocities, is defined as the length of the recirculation zone. The slip velocities decrease along the fore-cone until the locations $x = 0.076$ m, 0.77 m, 0765 m, and 0.80 m for the first order conditions $\sigma_u = \sigma_T = 1$, the case with $A_1 = 1$, $A_2 = 0.5$, $C_1 = 1$, $C_2 = 0.2$, the case with $\sigma_T = 1$, $A_1 = 1$, $A_2 = 0.5$ and DSMC data [19], respectively. The CFD results using the second order boundary conditions are close to DSMC data. The lengths of the recirculation zone are 1) 25.5 mm for the first order conditions $\sigma_u = \sigma_T = 1$, 2) 26.7 mm for the case with $A_1 = 1$, $A_2 = 0.5$, $C_1 = 1$, $C_2 = 0.2$, 3) 26.5 mm for the case with $\sigma_T = 1$, $A_1 = 1$, $A_2 = 0.5$ and 4) 20.8 mm for DSMC data. Past this zone, the slip velocities increase and oscillate along the second cone and there

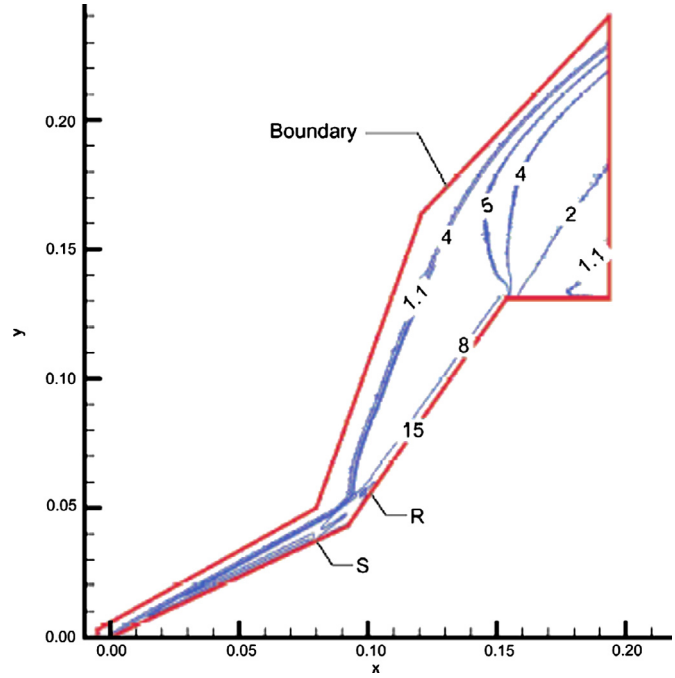

(a) DSMC

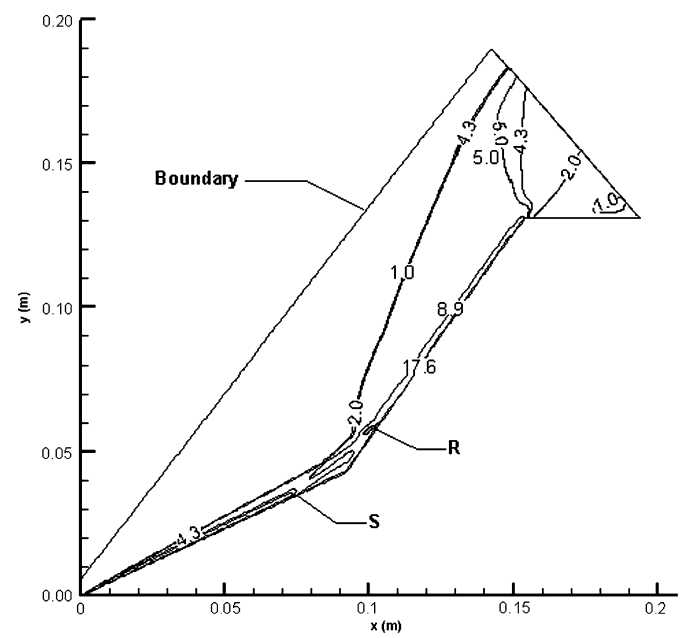

(b) Normalized density contours with the second order conditions

Fig. 27. Normalized density contours (ρ/ρ_∞) in computational domain of the biconic case (a) DSMC [19], and (b) second order conditions, $A_1 = 1$, $A_2 = 0.5$, $C_1 = 1$, $C_2 = 0.2$ (S: Separation; R: Re-attachment).

is good agreement between the CFD results and DSMC data in the range $0.105 \le x \le 0.156$. On the base surface ($0.156 \le x \le 0.1937$) the slip velocity predicted by the second order condition is close to DSMC data than that of the first order conditions. Over the whole biconic surface, the second order conditions predict better slip velocity than that of the first order conditions once comparing with DSMC data.

For completeness, the normalized density contours (ρ/ρ_∞) in the whole computational domain and the recirculation region are presented in Figs. 27 and 28, respectively. The normalized density contours of the second order conditions with $A_1 = 1$, $A_2 = 0.5$, $C_1 = 1$, $C_2 = 0.2$ are compared with DSMC normalized density con-

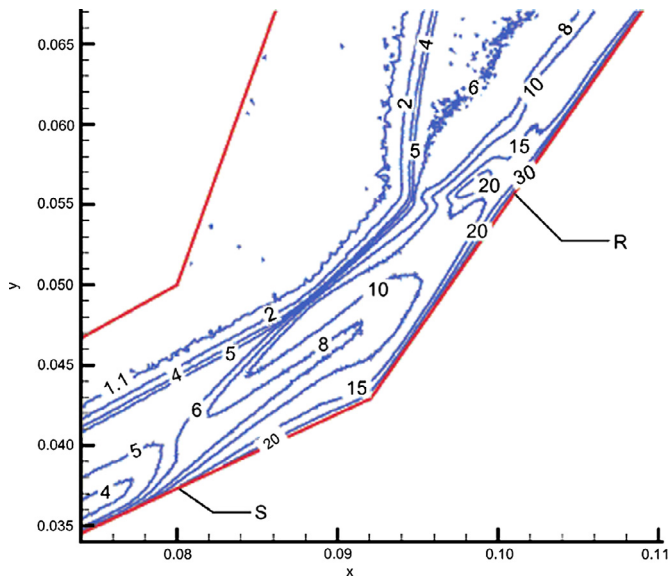

(a) DSMC

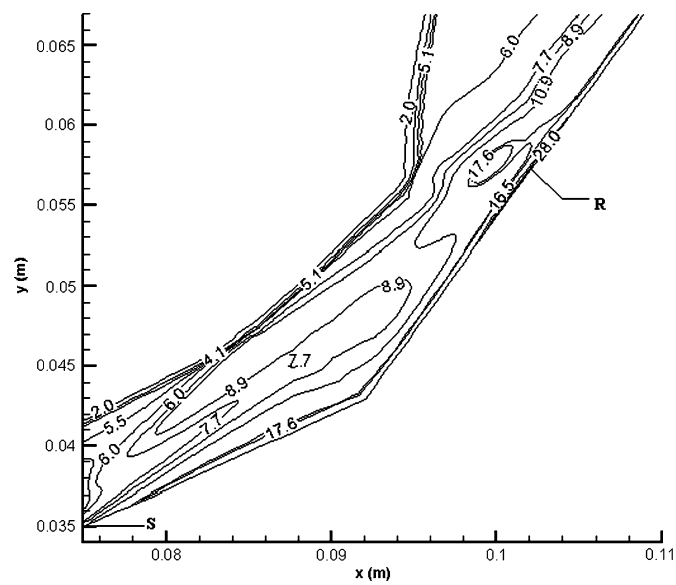

(b) Normalized density contours with the second order conditions

Fig. 28. Normalized density contours (ρ/ρ_∞) in the separation region of the biconic case (a) DSMC [19], and (b) second order conditions, $A_1 = 1$, $A_2 = 0.5$, $C_1 = 1$, $C_2 = 0.2$ (S: Separation; R: Re-attachment).

tours [19]. In Figs. 27a and 27b, normalized density contours of the second order conditions are slightly higher than those of DSMC at the boundary edge of the bow shock and near the biconic surface on the second cone beyond the separation zone. Figs. 28a and 28b present normalized density contours in the recirculation zone. The DSMC density contours are higher than those of the CFD using the second order conditions at near the surface (within the shock layer). This can be explained that the DSMC method produces large flowfield gradients due to shock interactions and substantial amplifications of surface loads caused by shock/boundary layer interactions [19]. Overall, the second order conditions are not superior to the first order conditions to predict the surface quantities for axis-symmetrical case.

7. Conclusions

The combination of the first order and the second order slip/jump boundary conditions was successfully employed with the N-S-F equations for simulating rarefied gas flows around the NACA 0012 airfoil and the sharp 25–55-deg biconic cases. The effects of the first and the second order terms (through evaluating different sets of the coefficients A_1, A_2, C_1, and C_2) on the behavior of the rarefied gas flows for the airfoil and biconic cases are also investigated by numerical simulations. The coefficients of the second order conditions are varied to match DSMC data for the most cases, except the slip velocity along the upper surface for the airfoil cases (AOA = 10-deg) by numerical difficulty associated with accurate calculations of the second order derivative of the velocity gradient normal to the curved surface due to increasing AOA. The combination of the second order slip and jump conditions predicts the surface gas temperature and drag coefficients better than those of the first order conditions in comparison with DSMC data for the airfoil cases. For the airfoil case, AOA = 10-deg, $M = 2$, the second order conditions give suitable agreement with DSMC data for the shear stress and slip velocity over the upper and lower airfoil surfaces, respectively. The simulation results of the heat transfer for the airfoil cases figure out that the difference between DSMC and CFD results is proportional to the increase in the free stream velocity. The simulation results of the biconic case point out that the second order conditions are not much better than the first order conditions for predicting surface quantities for the biconic case.

Conflict of interest statement

None declared here.

Acknowledgement

Nam T.P. Le would like to acknowledge the Ton Duc Thang University for financial support that supported this work.

References

[1] C.J. Roy, M.A. Gallis, T.J. Bartel, J.L. Payne, Navier–Stokes and DSMC simulations for hypersonic laminar shock–shock interaction flows, AIAA Paper 2002-0737, 2002.
[2] J.J. Bertin, R.M. Cummings, Critical hypersonic aerothermodynamic phenomena, Annu. Rev. Fluid Mech. 38 (2006) 129–157.
[3] J.R. Wilson, Mini technologies for major impact, Aerosp. Am. 36 (1998) 36–42.
[4] J. Fan, I.D. Boyd, C. Cai, Computation of rarefied gas flows around a NACA 0012 airfoil, AIAA J. 39 (2001) 618–625.
[5] OpenFOAM, http://www.openfoam.com, 08/2014.
[6] C.J. Greenshields, H.G. Weller, L. Gasparini, J.M. Reese, Nonoscillatory central schemes for high speed viscous flows, Int. J. Numer. Methods Fluids 23 (2010) 1–21.
[7] J. Allegre, M. Raffin, J.C. Lengrand, Experimental flowfields around NACA 0012 airfoils located in subsonic and supersonic rarefied air streams, in: Numerical Simulation of Compressible Navier–Stokes Flows, Vieweg and Sohn, Braunschweig, Germany, 1985, pp. 59–68.
[8] A. Shoja-Sani, E. Roohi, M. Kahrom, S. Stefanov, Investigation of aerodynamic characteristics of rarefied flow around NACA 0012 airfoil using DSMC and NS solvers, Eur. J. Mech. B, Fluids 48 (2014) 59–74.
[9] W. Hasse, Solution of the Navier–Stokes equations for sub- and supersonic flows in rarefied gases, in: Numerical Simulation of Compressible Navier–Stokes Flows, Vieweg and Sohn, Braunschweig, Germany, 1985, pp. 139–157.
[10] J. Allegre, N. Raffin, L. Gottesdient, Slip effect on supersonic flowfields around NACA 0012 airfoils, in: Proceedings of the Fifteenth of International Symposium on Rarefied Gas Dynamics, 1986, pp. 548–557.
[11] J.Y. Yang, J.C. Huang, C.S. Wang, Nonoscillatory schemes for kinetic model equations for gases with internal energy states, AIAA J. 34 (1996) 2071–2081.
[12] P.L. Bhatnagar, E.P. Gross, M. Krook, A model for collision processes in gases. I. Small amplitude processes in charged and neutral one component systems, Phys. Rev. 94 (1954) 511–525.
[13] T.F. Morse, Kinetic models for gases with internal degrees of freedom, Phys. Fluids 7 (1964) 159–169.
[14] L.H. Holway, New statistical models for kinetic theory: methods of construction, Phys. Fluids 9 (1966) 1658–1673.
[15] I. Nompelis, G.V. Candler, US3D predictions of double-cone and hollow cylinder-flare flows at high enthalpy, AIAA Paper 2014-3366, 2014.

[16] M.S. Holden, T.P. Wadhams, G.V. Candler, J.K. Harvey, Measurements in regions of low density laminar shock wave/boundary layer interaction in hypervelocity flows and comparison with Navier–Stokes predictions, AIAA Paper 2003-1131, 2003.
[17] M.S. Holden, T.P. Wadhams, Code validation study of laminar shock/boundary layer and shock/shock interactions in hypersonic flow Part A: experimental measurements, AIAA Paper 2001-1031, 2001.
[18] S.M. Ruffin, Prediction of vibrational relaxation in hypersonic expanding flows Part 1: model development, J. Thermophys. Heat Transf. 9 (1995) 432–437.
[19] J.N. Moss, G.A. Bird, Direct Simulation Monte Carlo simulations of hypersonic flows with shock interactions, AIAA J. 43 (2005) 2565–2573.
[20] M.C. Druguet, G.V. Candler, I. Nompelis, Effect of numerics on Navier–Stokes computations of hypersonic double-cone flows, AIAA J. 4 (2005) 616–623.
[21] J.K. Harvey, A review of a validation exercise on the use of the DSMC method to compute viscous/inviscid interactions in hypersonic flow, AIAA Paper 2003-3643, 2003.
[22] E. Titov, J. Burt, E. Josyula, I. Nompelis, Implications of slip boundary conditions on surface properties in hypersonic flows, AIAA Paper 2012-3307, 2012.
[23] J.C. Maxwell, On stresses in rarefied gases arising from inequalities of temperature, Philos. Trans. R. Soc. Part 1 170 (1879) 231–256.
[24] M. von Smoluchowski, Überwärmeleitung in verdünntengasen, Ann. Phys. Chem. 64 (1898) 101–130.
[25] E.H. Kennard, Kinetic Theory of Gases, McGraw-Hill, 1938.
[26] K.B. Jordan, Direct numeric simulation of shock wave structures without the use of artificial viscosity, PhD thesis, Marquette University, 2011.
[27] K. Yun, R.K. Agarwal, R. Balakrishman, Hypersonic flow computations in the continuum-transition regime using the augmented Burnett and BGK Burnett equations, in: Proceedings of the Sixteenth International Conference Numerical Methods Fluid Dynamics, in: Lecture Notes in Physics, vol. 515, 1998, pp. 560–565.
[28] D.A. Lockerby, J.M. Reese, D.R. Emerson, R.W. Barber, Velocity boundary condition at solid walls in rarefied gas calculations, Phys. Rev. E 70 (2004) 017303.
[29] R.G. Deissler, An analysis of second order slip flow and temperature jump boundary conditions for rarefied gases, Int. J. Heat Mass Transf. 7 (1964) 681–694.
[30] N.T.P. Le, E. Roohi, Second order temperature boundary condition for hypersonic and microscale rarefied gas flows, in: Proceedings of the Twenty-Ninth of International Symposium on Rarefied Gas Dynamics, vol. 1628, 2014, pp. 374–381.
[31] N.T.P. Le, C.J. Greenshields, J.M. Reese, Evaluation of nonequilibrium boundary condition in simulating hypersonic gas flows, Progr. Flight Phys. 3 (2012) 217–230.
[32] G.A. Bird, The DSMC Method, Clarendon, Oxford, 2013.
[33] A. Lofthouse, L.C. Scalabrin, I.D. Boyd, Velocity slip and temperature jump in hypersonic aerothermodynamics, J. Thermophys. Heat Transf. 22 (2008) 38–49.
[34] I.H. Abbott, A.E. von Doenhoff, Theory of Wing Sections, Including a Summary of Airfoil Data, McGraw Hill, 1949.
[35] I.D. Boyd, G. Chen, V.C. Candler, Predicting failure of the continuum fluid equations in transitional hypersonic flows, Phys. Fluids 7 (1995) 210–219.
[36] M.J. Martin, I.D. Boyd, Momentum and heat transfer in a laminar boundary layer with slip flow, J. Thermophys. Heat Transf. 20 (2006) 710–719.
[37] C. Cercignani, Mathematical Methods in Kinetic Theory, Plenum, New York, 1969.
[38] J. Maurer, P. Tabeling, P. Joseph, H. Willaime, Second-order slip laws in microchannels for helium and nitrogen, Phys. Fluids 15 (2003) 2613–2621.
[39] D.A. Lockerby, J.M. Reese, D.R. Emerson, R.W. Barber, Velocity boundary condition at solid walls in rarefied gas calculations, Phys. Rev. E 70 (2004) 017303.
[40] N. Dongari, A. Agrawal, A. Agrawal, Analytical solution of gaseous slip flow in long microchannels, Int. J. Heat Mass Transf. 50 (2007) 3411–3421.
[41] W. Zhang, G. Meng, X. Wei, A review on slip models for gas microflows, Microfluid. Nanofluid. 13 (2012) 845–882.
[42] G.A. Radtke, N.G. Hadjiconstantinou, S. Takataand, K. Aoki, On the second-order temperature jump coefficient of a dilute gas, J. Fluid Mech. 707 (2012) 331–341.